The Astrophysical Journal Letters, 902:L36 (14pp), 2020 October 20 https://doi.org/10.3847/2041-8213/abbadd

Constraints from Gravitational-wave Detections of Binary Black Hole Mergers on the $^{12}C(\alpha, \gamma)^{16}O$ Rate

R. Farmer[1,2], M. Renzo[3], S. E. de Mink[1,2], M. Fishbach[4], and S. Justham[1,5,6]
[1] Anton Pannekoek Institute for Astronomy and GRAPPA, University of Amsterdam, NL-1090 GE Amsterdam, The Netherlands; r.j.farmer@uva.nl
[2] Center for Astrophysics | Harvard & Smithsonian, 60 Garden Street, Cambridge, MA 02138, USA
[3] Center for Computational Astrophysics, Flatiron Institute, New York, NY 10010, USA
[4] Department of Astronomy and Astrophysics, University of Chicago, Chicago, IL 60637, USA
[5] School of Astronomy & Space Science, University of the Chinese Academy of Sciences, Beijing 100012, People's Republic of China
[6] National Astronomical Observatories, Chinese Academy of Sciences, Beijing 100012, People's Republic of China
Received 2020 June 5; revised 2020 September 8; accepted 2020 September 23; published 2020 October 19

Abstract

Gravitational-wave detections are starting to allow us to probe the physical processes in the evolution of very massive stars through the imprints they leave on their final remnants. Stellar evolution theory predicts the existence of a gap in the black hole mass distribution at high mass due to the effects of pair instability. Previously, we showed that the location of the gap is robust against model uncertainties, but it does depend sensitively on the uncertain $^{12}C(\alpha, \gamma)^{16}O$ rate. This rate is of great astrophysical significance and governs the production of oxygen at the expense of carbon. We use the open-source MESA stellar evolution code to evolve massive helium stars to probe the location of the mass gap. We find that the maximum black hole mass below the gap varies between 40 $M_{\odot}$ and 90 $M_{\odot}$, depending on the strength of the uncertain $^{12}C(\alpha, \gamma)^{16}O$ reaction rate. With the first 10 gravitational-wave detections of black holes, we constrain the astrophysical S-factor for $^{12}C(\alpha, \gamma)^{16}O$, at 300 keV, to $S_{300} > 175$ keV b at 68% confidence. With $\mathcal{O}(50)$ detected binary black hole mergers, we expect to constrain the S-factor to within $\pm$10–30 keV b. We also highlight a role for independent constraints from electromagnetic transient surveys. The unambiguous detection of pulsational pair-instability supernovae would imply that $S_{300} > 79$ keV b. Degeneracies with other model uncertainties need to be investigated further, but probing nuclear stellar astrophysics poses a promising science case for the future gravitational-wave detectors.

Unified Astronomy Thesaurus concepts: Stellar evolution (1599); Supernovae (1668); Core-collapse supernovae (304); Nuclear astrophysics (1129); Stellar mass black holes (1611); Astrophysical black holes (98); Massive stars (732); Late stellar evolution (911)

1. Introduction

The $^{12}C(\alpha, \gamma)^{16}O$ reaction is one of the most important nuclear reaction rates (Burbidge et al. 1957) in the evolution of stars yet also one of the most uncertain (Holt et al. 2019). Reducing the uncertainty on this rate has been dubbed "the holy grail of nuclear astrophysics" (deBoer et al. 2017; Bemmerer et al. 2018). It plays a key role in governing the evolution and composition of stars beyond the main sequence, from the C/O ratio in white dwarfs (Salaris et al. 1997; Straniero et al. 2003; Fields et al. 2016), to whether a star will form a neutron star or a black hole (Brown et al. 2001; Heger et al. 2002; Woosley et al. 2002; Tur et al. 2007; West et al. 2013; Sukhbold & Adams 2020), and the amount of ^{12}C and ^{16}O in the universe (Boothroyd & Sackmann 1988; Weaver & Woosley 1993; Thielemann et al. 1996).

Thus improving our understanding of this key rate is of critical importance to stellar astrophysics. The difficulty in measuring the rate occurs due to the negligible cross section of the reaction at temperatures relevant for helium burning in stars (An et al. 2015, 2016). Thus nuclear experiments can only provide data for much higher energies (i.e., temperatures), from which we extrapolate down to astrophysically relevant energies. However, the cross section has a complex energy dependence and thus is not easily extrapolated to lower temperatures (deBoer et al. 2017; Friščić et al. 2019). Recent lab measurements, with high beam luminosities, have begun to reduce the uncertainty on the rate through indirect studies of the excited states of ^{16}O and improved theoretical modeling of the $^{12}C(\alpha, \gamma)^{16}O$ rate (Hammer et al. 2005; An et al. 2016; Hammache et al. 2016; deBoer et al. 2017; Shen et al. 2020). New experiments will soon be better able to probe the $^{12}C(\alpha, \gamma)^{16}O$ reaction rate at astrophysically relevant temperatures (Holt et al. 2018; Friščić et al. 2019).

Astrophysical studies using white dwarfs have attempted to place constraints on the $^{12}C(\alpha, \gamma)^{16}O$ reaction rate using asteroseismology of white dwarfs (Metcalfe et al. 2001, 2002; Metcalfe 2003). However, these measurements are sensitive to other physics choices, such as semiconvection and convective overshoot mixing (Straniero et al. 2003), which are poorly constrained. Thus a cleaner signal is needed to provide a more robust estimate from stellar astrophysical sources.

Merging black holes detected by LIGO/Virgo (Acernese et al. 2015; LIGO Scientific Collaboration et al. 2015) can provide such a signal, via the location of the pair-instability mass gap (Takahashi 2018; Farmer et al. 2019). A gap is predicted to form in the mass distribution of black holes, due to pair-instability supernovae (PISNe) completely disrupting massive stars, leaving behind no remnant (Fowler & Hoyle 1964; Barkat et al. 1967; Woosley 2017). The lower edge of the gap is set by mass loss experienced by a star during a pulsational PISN (PPISN) (Rakavy & Shaviv 1967; Fraley 1968; Woosley et al. 2002). These objects undergo multiple phases of mass loss before collapsing into a black hole (Woosley et al. 2002; Chen et al. 2014; Yoshida et al. 2016; Woosley 2017; Farmer et al. 2019; Marchant et al. 2019).

In Farmer et al. (2019) we evolved hydrogen-free helium cores and found that the lower edge of the PISN black hole

mass gap was robust to changes in the metallicity and other uncertain physical processes, e.g., wind mass loss and chemical mixing. Over the range of metallicities considered, the maximum black hole mass decreased by 3 $M_\odot$. We also showed that the choices for many other uncertain physical processes inside stars do not greatly affect the location of the PISN mass gap.

The existence of a gap in the mass distribution of merging binary black holes (BBHs) would provide strong constraints on their progenitors, and hence on the post-main-sequence evolution of stars, which includes the effect of $^{12}C(\alpha, \gamma)^{16}O$ on a star's evolution (Takahashi 2018; Sukhbold & Adams 2020). The existence of a gap in the mass distribution can also be used as a "standardizable siren" for cosmology and used to place constraints on the Hubble constant (Schutz 1986; Holz & Hughes 2005; Farr et al. 2019).

Here we investigate how the maximum black hole mass below the PISN mass gap is sensitive to the $^{12}C(\alpha, \gamma)^{16}O$ nuclear reaction rate and thus can be used to place constraints on the reaction rate. In Section 2 we discuss our methodology. In Section 3 we describe the star's evolution before pulsations begin, and how this is altered by the $^{12}C(\alpha, \gamma)^{16}O$ reaction rate. In Section 4 we show how the maximum black hole mass below the gap is affected by the nuclear redaction rates, and we place constraints on the $^{12}C(\alpha, \gamma)^{16}O$ reaction rate in Section 5. In Section 6 we discuss how these results will improve with future gravitational-wave detections. In Section 7 we discuss potentially other observables that can be used to constrain the $^{12}C(\alpha, \gamma)^{16}O$ rate. Finally, in Sections 8 and 9, we discuss and summarize our results.

2. Method

There are many channels for the formation of a source detectable by ground-based gravitational-wave detectors. We consider here the case where the progenitors of the merging black holes have come from an isolated binary system. There are multiple stellar pathways for this to produce a successful BBH merger, including common-envelope evolution (Tutukov & Yungelson 1993; Dominik et al. 2012; Belczynski et al. 2016b), chemically homogeneous evolution (de Mink & Mandel 2016; Mandel & de Mink 2016; Marchant et al. 2016), and stars that interact in dynamic environments (Kulkarni et al. 1993; Portegies Zwart & McMillan 2000; Gerosa & Berti 2019) In each case, we expect the stars to lose their hydrogen envelopes after the end of their main sequence, leaving behind the helium core of each star.

We use the MESA stellar evolution code, version 11701 (Paxton et al. 2011, 2013, 2015, 2018, 2019), to follow through the various stages of nuclear burning inside these helium cores until they either collapse to form a black hole or explode as a PISN. We follow the evolution of helium cores with initial masses between $M_{\rm He,init} = 30\,M_\odot$ and $M_{\rm He,init} = 200\,M_\odot$ in steps of 1 $M_\odot$, at a metallicity of $Z = 10^{-5}$. We use the default model choices from Farmer et al. (2019) for setting all other MESA input parameters. See Appendix A for further details of our usage of MESA; our input files with all the parameters we set can be found in Zenodo at doi:10.5281/zenodo.3559859.

After a star has formed its helium core, it begins burning helium in its central region, converting ^{4}He into ^{12}C and then ^{16}O. The final ratio of the mass fractions of ^{12}C and ^{16}O depends on the relative strengths of the 3α reaction rate, which produces ^{12}C, and the $^{12}C(\alpha, \gamma)^{16}O$ reaction rate, which converts the ^{12}C into ^{16}O. We define the end of core helium burning to occur when the central mass fraction of ^{4}He drops below 10^{-4}. The core is now dominated by ^{12}C and ^{16}O, with only trace mass fractions of other nuclei. This core then begins a phase of contraction, and thermal neutrino losses begin to dominate the total energy loss from the star (Fraley 1968; Heger et al. 2003, 2005; Farmer et al. 2016).

As the core contracts, the central density and temperature increase, which, for a sufficiently massive core, causes the core to begin producing copious amounts of electron–positron pairs ($e^\pm$). The production of the $e^\pm$ removes photons, which were providing pressure support, softening the equation of state (EOS) in the core, and causes the core to contract further. We then follow the dynamical collapse of the star, which can be halted by the ignition of oxygen, leading to either a PPISN or a PISN. We follow the core as it contracts and bounces (Marchant et al. 2019), generating shock waves that we follow through the star until they reach its outer layers. These shocks then cause mass loss from the star, as material becomes unbound. In this case we find that the star can eject between 0.1 $M_\odot$ and $\sim$20 $M_\odot$ of material in a pulsational mass loss episode (Woosley 2017; Farmer et al. 2019; Renzo et al. 2020a). Stars at the boundary between core collapse and PPISN may generate weak pulses, due to only a small amount of material becoming dynamically unstable, and therefore do not drive any appreciable mass loss (Woosley 2017). We use the term PPISN only for an event that ejects mass (Renzo et al. 2020a). PISNe are stars for which the energy liberated by the thermonuclear explosion of oxygen (and carbon) exceeds the total binding energy, resulting in total disruption after only one mass loss episode.

As a star evolves into the pair-instability region we switch to using MESA's Riemann contact solver, HLLC (Toro et al. 1994; Paxton et al. 2018), to follow the hydrodynamical evolution of each pulse. This switch occurs when the volumetric pressure-weighted average adiabatic index $\langle\Gamma_1\rangle - 4/3 < 0.01$, which occurs slightly before the star enters the pair-instability region. The adiabatic index, Γ_1, is defined as

$$\Gamma_1 = \left.\frac{d\ln P}{d\ln \rho}\right|_s \tag{1}$$

where P and ρ are the local pressure and density, and their logarithmic ratio is evaluated at a constant entropy s. We used the continuity equation to transform the volumetric integral of Γ_1 into an integral over the mass domain, thus (Stothers 1999)

$$\langle\Gamma_1\rangle \equiv \frac{\int \Gamma_1 P\, d^3r}{\int P\, d^3r} \equiv \frac{\int \Gamma_1 \frac{P}{\rho}\, dm}{\int \frac{P}{\rho}\, dm}. \tag{2}$$

We follow the dynamical evolution of the star until all shocks have reached its surface. These shocks may unbind a portion of the outer stellar envelope, resulting in mass loss (Yoshida et al. 2016; Woosley 2019; Renzo et al. 2020a). We follow the ejected material until the bound portion of the star relaxes back into hydrostatic equilibrium, after it has radiated away the energy of the pulse. We remove the material that has become unbound from our computational grid by generating a new stellar model with the same entropy and chemical distribution as the remaining bound material. We evolve this new star assuming hydrostatic equilibrium until either another pulse occurs or the core temperature (T_c) exceeds $T_c > 10^{9.6}$ K, as the star is approaching core collapse. At this point we switch back to using the

hydrodynamic solver. We define the final core collapse to occur when any part of the star begins collapsing with a velocity $v > 8000$ km s^{-1}, so that any pulse that is in the process of being ejected during core collapse is resolvable.

Stars with core masses above $M_{\rm He,init} \gtrsim 120\,M_\odot$ attempt to undergo a PISN; however, sufficient energy is released during the pulse that the core heats to the point where photodisintegrations become the dominant energy sink. These reactions then reduce the available energy, which was powering the outward moving shock, and prevent the envelope from becoming unbound. The star then collapses without significant mass loss. We assume that it forms a black hole (Bond et al. 1984; Woosley 2017).

We define the mass of the black hole formed to be the mass of the bound material of the star at collapse. Given the uncertain mechanism of black hole formation (Fryer 1999; Fryer et al. 2001, 2012), or weak shock generation (Nadezhin 1980; Lovegrove & Woosley 2013; Fernández et al. 2018), our black holes masses are upper limits. We take the bound mass rather than the total mass because some stars are undergoing a mass ejection from a pulsation at the time of core collapse (Renzo et al. 2020a).

2.1. Nuclear Reaction Rates

Nuclear reaction rates play a key role in the evolution and final fate of a star. However, they are also uncertain and this uncertainty varies as function of temperature (Iliadis et al. 2010a, 2010b; Longland et al. 2010). Varying nuclear reaction rates within their known uncertainties has been shown to a have large impact on the structure of a star (Hoffman et al. 1999; Iliadis et al. 2002).

To sample nuclear reaction rates within their known uncertainties, we use the STARLIB (Sallaska et al. 2013) (version 67a) library. STARLIB provides both the median reaction rate and uncertainty in that reaction as a function of temperature. We sample each reaction at a fixed number of standard deviations from the median (Evans et al. 2000). We assume that the temperature-dependent uncertainty in a reaction follows a log-normal distribution (Longland et al. 2010).

For each reaction rate tested, we create a sampled reaction rate at 60 points log-spaced in temperature between $0.01 \leqslant {\rm T/GK} \leqslant 10$ (Fields et al. 2016, 2018).

The rate of a reaction per particle pair is given by

$$N_{\rm A}\langle\sigma\nu\rangle = \left(\frac{8}{\pi\mu}\right)^{1/2}\frac{N_{\rm A}}{(k_{\rm B}T)^{3/2}} \times \int_0^\infty \sigma(E)E\,\exp(-E/k_{\rm B}T)\,dE \quad (3)$$

where μ is the reduced mass of the particles, $E = \mu\nu^2/2$ is the center-of-mass energy, ν is the average velocity of the particles, $N_{\rm A}$ is Avogadro's number, and $k_{\rm B}$ is the Boltzmann constant (e.g., deBoer et al. 2017; Lippuner & Roberts 2017; Holt et al. 2019). We can factor out the energy-dependent cross section $\sigma(E)E$ by replacing it with the astrophysical S-factor:

$$S(E) = \sigma(E)E\,e^{2\pi\eta} \quad (4)$$

and

$$\eta = \sqrt{\frac{\mu}{2E}}Z_1Z_2\frac{e^2}{\hbar} \quad (5)$$

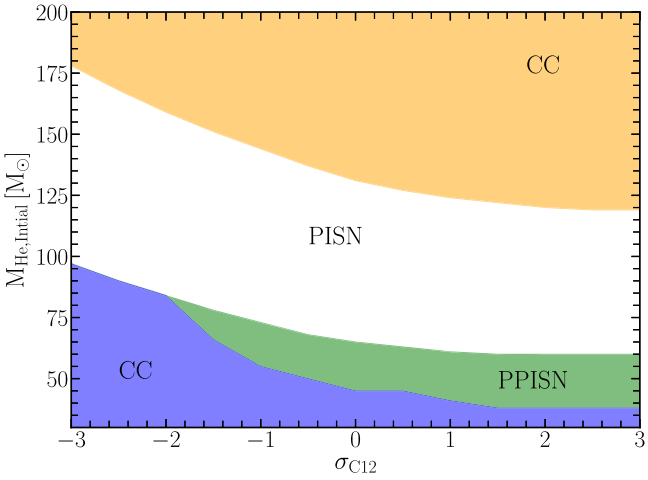

Figure 1. Final fate of a star as a function of the initial helium core mass and ^{12}C(α, γ)^{16}O rate. $\sigma_{\rm C12}$ denotes how far the ^{12}C(α, γ)^{16}O rate is from the median STARLIB rate, measured in standard deviations. Blue regions indicate stars that undergo core collapse (CC) below the PISN mass gap, green regions form black holes after a PPISN, while white regions are completely disrupted in a PISN, and models in the orange region form black holes from core collapse for stars above the PISN mass gap. There are 2210 models in the grid spaced by 1 $M_\odot$ and 0.5$\sigma_{\rm C12}$.

where η is the Sommerfeld parameter, $Z_{1,2}$ is the proton charge of each particle, e is the electric charge, and $\hbar$ is the reduced Planck's constant. The $e^{2\pi\eta}$ term accounts for (approximately) the influence of the Coulomb barrier on the cross section. As the S-factor depends on energy, we quote it at the typical energy for a reaction. For ^{12}C(α, γ)^{16}O the typical energy is $E = 300$ keV.

3. Pre-SN Carbon Burning

In Figure 1 we show the outcome for our grid of 2210 evolutionary models as a function of the initial helium core mass and the ^{12}C(α, γ)^{16}O reaction. We parameterize the ^{12}C(α, γ)^{16}O reaction in terms of the number of sigmas ($\sigma_{\rm C12}$) from the median STARLIB ^{12}C(α, γ)^{16}O reaction rate:

$$\langle\sigma\nu\rangle = \langle\sigma\nu\rangle_{\rm median}\,e^{\mu(T)\sigma_{\rm C12}} \quad (6)$$

where $\langle\sigma\nu\rangle_{\rm median}$ is the median reaction rate provided by STARLIB, and $\mu(T)$ is the temperature-dependent uncertainty in the reaction (which is assumed to follow a log-normal distribution).

For higher initial core mass (for a given ^{12}C(α, γ)^{16}O rate), the final fate of a star transitions from core collapse to PPISN, to PISN, and then to core collapse again (Bond et al. 1984). As the reaction rate increases (i.e., large values of $\sigma_{\rm C12}$), the boundary between the different final fates shifts to lower initial helium core mass. See Section 7 for a discussion of the implications of this for the rate of black hole formation and the electromagnetic transient rate.

To understand the reason for these trends, it is insightful to consider the ^{12}C mass fraction in the core of the stellar models after core helium burning has finished. We define the end of core helium burning to be when the mass fraction of ^{4}He at the center of the star drops below 10^{-4}. Figure 2 shows that the ^{12}C mass fraction in the core of the stars considered here decreases from ≈30% to ≈0.001% as the ^{12}C(α, γ)^{16}O rate is increased from $\sigma_{\rm C12} = -3$ to $\sigma_{\rm C12} = 3$, independent of initial mass. This change in the ^{12}C mass fraction is what drives the changes in the star's later phases of evolution and thus its final fate.

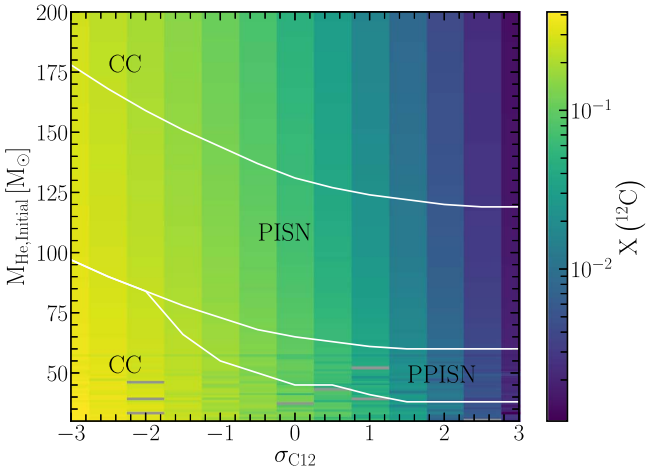

Figure 2. The mass fraction of ^{12}C in the core after core helium burning, but before carbon burning, for all initial masses as a function of σ_{C12}. White lines denote the boundaries between the different final fates. Text labels denote the final fate of the star. Gray boxes denote models that do not evolve beyond core helium burning, defined as when the mass fraction of ^{4}He at the center of the star drops below 10^{-4}.

After core helium burning has ceased the core begins to contract, increasing its density and temperature. However, at the same time, thermal neutrino losses increase, which acts to cool the core. The next fuel to burn is ^{12}C via ^{12}C + ^{12}C to ^{22}Ne, ^{23}Na, and ^{24}Mg (Arnett & Truran 1969; Farmer et al. 2015). As the ^{12}C + ^{12}C reaction rate depends on the number density of carbon squared, small changes in the number density can have a large impact on the power generated by the reaction.

In Figure 3 we show a simplified picture of the steps a star takes to its final fate depending on its ^{12}C(α, γ)^{16}O reaction rate. The top panel shows a star that would undergo core collapse, by igniting carbon first at the center and then in an off-center shell. This star then avoids igniting oxygen explosively and instead proceeds through its evolution to core collapse. As the ^{12}C(α, γ)^{16}O rate increases, the carbon stops igniting at the center and only ignites in a shell (middle panel), before proceeding to ignite oxygen explosively. For the highest ^{12}C(α, γ)^{16}O rate shown, no carbon is burnt before oxygen ignites (bottom panel). The C/O ratios shown are defined at the end of core helium burning.

The reason why changing the carbon burning behavior changes the final outcome for a star can be seen in Figure 4. Here we show the time evolution of the helium cores, for stars with $M_{\rm He,init} = 60\,M_\odot$ during carbon burning and up to the ignition of oxygen, for different ^{12}C(α, γ)^{16}O rates. The top row shows a Kippenhahn diagram of the time evolution of the net nuclear energy minus neutrino losses and the mixing regions inside the star. The middle row shows the evolution of $\Gamma_1 - 4/3$. Regions where $\Gamma_1 - 4/3 < 0$ are locally unstable. The bottom row shows the temperature and density structure inside the star at points in time marked on the top row of Figure 4. The points in time marked show how the stars are evolving on different timescales. Timescales vary from a few thermal timescales (left column) to a few dynamical timescales (middle and right columns).

When the ^{12}C(α, γ)^{16}O rate is small (and thus the ^{12}C mass fraction is $\approx$30%, with the rest of the core being made of ^{16}O), ^{12}C ignites vigorously at the center in a radiative region (Figure 4 top left) and burns outward until it begins to drive a convective ^{12}C burning shell. The star will then ignite oxygen in the core (non-explosively) and proceed through silicon and iron burning before collapsing in a core collapse.

As the ^{12}C(α, γ)^{16}O rate increases, the initial ^{12}C ignition point, defined where the nuclear energy generated is greater than the energy lost in neutrinos, moves outward in mass coordinate (Figure 4 top center). As the ^{12}C abundance decreases, the star requires a higher density to burn ^{12}C vigorously, and thus it must contract further, which increases the neutrino losses. No convective carbon shell forms before the oxygen in the core ignites explosively and the star proceeds to a PPISN. Once the ^{12}C(α, γ)^{16}O rate increases sufficiently such that the core is depleted in ^{12}C after core helium burning, no ^{12}C burning region forms and the core proceeds to ignite oxygen explosively (Figure 4 top right) as a PISN, leaving behind no black hole remnant.

Stars with a convective ^{12}C burning shell can resist the collapse caused by the production of $e^{\pm}$ and thus maintain hydrostatic equilibrium until core collapse. Figure 4 (middle left) shows that when the shell forms it prevents the center of the star from reaching $\Gamma_1 - 4/3 < 0$. Therefore, the instability is only local and never becomes global: only a small region around the carbon shell becomes unstable. For stars without the convective carbon shell (middle center and middle right), a significant fraction of the entire star becomes unstable, resulting in a global instability.

Carbon burning begins at the center and moves outward (either vigorously or not), thus depleting the center of ^{12}C. Therefore, the carbon shell (if it forms) cannot move inwards because there is insufficient fuel for it to burn. The region undergoing carbon burning cannot move outward either, because the convection zone is mixing the energy released from the nuclear reactions over a significant portion of the star. This prevents layers above the carbon-burning region from reaching sufficient temperatures and densities for vigorous carbon burning (Farmer et al. 2015; Takahashi 2018).

The convective carbon shell can only be sustained then if it can bring fresh fuel in via convective mixing from the rest of the core. Thus when a convective carbon shell forms it also allows additional fuel to be mixed into the burning region from the outer layers of the core. This prolongs the lifetime of the carbon-burning shell and prevents the collapse due to $e^{\pm}$ from occurring until the carbon shell convective region is depleted in ^{12}C, which may not occur before the star undergoes core collapse.

As the carbon fraction decreases, the carbon shell burning becomes less energetic (because the ^{12}C + ^{12}C reaction rate depends on the density of carbon squared). Therefore, as σ_{C12} increases (and ^{12}C fraction decreases) less energy is released from the carbon burning, thus the fraction of the core where $\Gamma_1 - 4/3 < 0$ increases. There comes a critical point where the carbon burning is insufficient to prevent the violent ignition of oxygen in the core, thus pulsations begin. Around this critical region, convective carbon burning can still occur, but the burning region can undergo flashes, where the ^{12}C ignites but is then quenched. This leads to weaker and shorter-lived convection zones, which do not mix in sufficient ^{12}C to sustain a continuous carbon-burning shell. This leads to very weak pulses removing only a few tenths of a solar mass of material. For stars with these weak convection zones the carbon shell only delays the ignition of oxygen; once carbon is sufficiently depleted the oxygen can ignite explosively. Eventually no

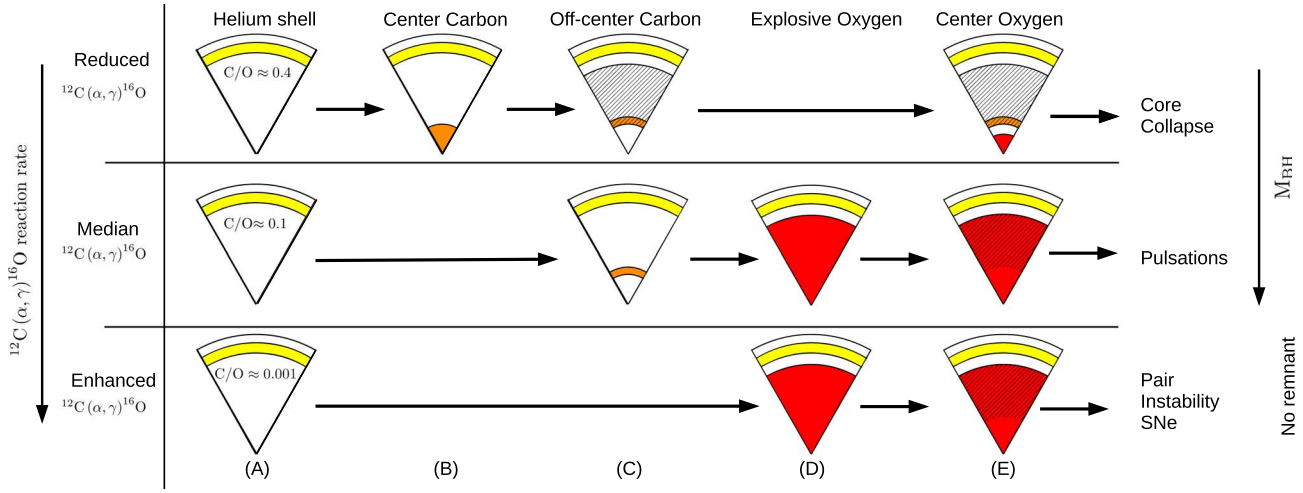

Figure 3. A schematic of the time progression of the major fuel burning, for a star with $M_{\rm He,init} = 60\,M_\odot$ as a function of $\sigma_{\rm C12}$, at reduced ($\sigma_{\rm C12} = -3$), median ($\sigma_{\rm C12} = 0$), and enhanced ($\sigma_{\rm C12} = 3$) ^{12}C(α, γ)^{16}O reaction rates. Yellow regions denote helium burning, orange regions denote carbon burning, and red regions denote oxygen burning. Hatched regions indicate convection mixing. Letters match those points marked in Figure 4. Also shown is the core's C/O mass ratio at the end of core helium burning.

carbon shell convection zone is formed at all (Figure 4 middle center); this leads to larger pulses removing solar masses of material.

The bottom row of Figure 4 shows the temperature–density profile inside the star at moments marked in the top row of Figure 4. As the stars evolve the core contracts and heats up; eventually the central regions of the star enter the instability region ($\Gamma_1 - 4/3 < 0$). Once a convective carbon shell forms (bottom left) the core stops contracting homogeneously (along the line where the radiation pressure is equal to the gas pressure) and moves to higher densities. This is due to the continued loss of entropy to neutrinos from the core. Thus when oxygen ignites, the core is outside the instability region ($\Gamma_1 - 4/3 > 0$) and as such does not undergo pulsational mass loss (Takahashi 2018).

For stars without a convective carbon shell (bottom center and bottom right) the core continues to contract homogeneously. When oxygen ignites it does so inside the $\Gamma_1 - 4/3 < 0$ region. As the temperature increases, due to the oxygen burning, the production of $e^{\pm}$ increases, causing a positive feedback loop. This leads to the explosive ignition needed to drive a pulse. Stars undergoing a PPISN (bottom center) have slightly lower core entropies than stars undergoing a PISN (bottom right) due to the small amount of non-convective carbon burning that occurs before oxygen burning begins.

Further decreases in the carbon abundance leave little carbon fuel to burn. Thus as the star collapses due to the production of $e^{\pm}$, the oxygen is free to ignite violently. This causes the star to undergo a PISN, which completely disrupts it. This can also be seen in Figure 2 where the boundaries between the different final fates move to lower masses as $\sigma_{\rm C12}$ increases, as the pulses become more energetic for a given initial mass.

3.1. Black Holes above the PISN Mass Gap

Figure 1 shows the population of black holes that form above the PISN mass gap. These black holes form due to the failure of the PISN explosion to fully unbind the star (e.g., Bond et al. 1984). As the helium core mass is increased (at constant $\sigma_{\rm C12}$) a PISN explosion increases in energy, due to a greater fraction of the oxygen being burnt in the oxygen ignition. This increased energy leads to an increase in the maximum core temperature the star reaches before the inward collapse is reverted and the star becomes unbound. This increased temperature can be seen in the increased production of ^{56}Ni as the initial mass increases (Woosley et al. 2002; Renzo et al. 2020a). Eventually the core reaches a sufficient temperature that the energy extracted from the core by photodisintegrations is sufficient to prevent the star from becoming unbound.

Figure 1 shows that as $\sigma_{\rm C12}$ increases, the initial helium core mass needed to form a black hole above the gap decreases. This is due to the increased production of oxygen as $\sigma_{\rm C12}$ increases. At these masses we do not see the formation of a convective carbon shell, even for $\sigma_{\rm C12} = -3$, though some radiative carbon burning occurs (similar to point C in the middle panels of Figure 4). Instead the cores with greater total amounts of oxygen can liberate greater amounts of energy from the oxygen burning. This burning raises the temperature in the core, allowing additional nucleosynthesis to occur with the silicon and iron group elements produced from the oxygen burning. For a fixed initial helium core mass as $\sigma_{\rm C12}$ increases, the peak core temperature increases. Once a core reaches $\log(T/{\rm K}) \approx 9.86$, then the rate of photodisintegrations is sufficient to prevent the star from unbinding itself. This is what sets the upper edge of the mass gap.

4. Edges of the PISN Mass Gap

Figure 5 shows the location of the PISN black hole mass gap as a function of the temperature-dependent uncertainty in ^{12}C(α, γ)^{16}O. As the rate increases (with increasing $\sigma_{\rm C12}$) both the lower and upper edges of the PISN mass gap shift to lower masses, from $\approx$90 $M_\odot$ to $\approx$40 $M_\odot$ for the lower edge and from $\approx$175 $M_\odot$ to $\approx$120 $M_\odot$ for the upper edge. The width of the region remains approximately constant at $83^{+5}_{-8}\,M_\odot$. The typical quoted value for the maximum mass of a black hole below the PISN mas gap is 45–55 $M_\odot$ (Yoshida et al. 2016; Woosley 2017; Farmer et al. 2019; Leung et al. 2019; Marchant et al. 2019). The gray box in Figure 5 shows the region of black hole masses, $M_{\rm BH} \approx 90$–$120\,M_\odot$, where we cannot place a black hole from a first-generation core collapse or PPISN model. Thus black holes detected in this mass region would need to

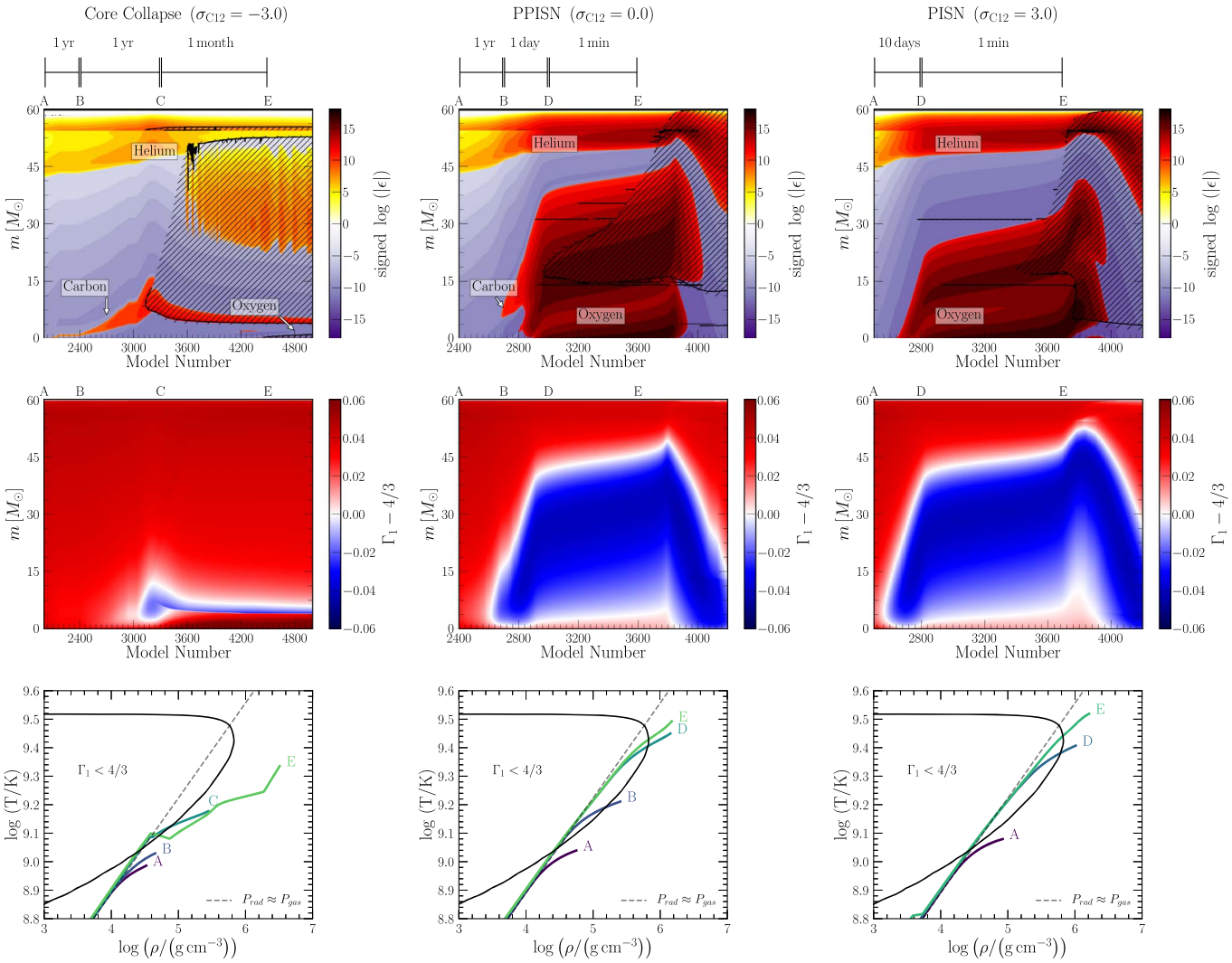

Figure 4. The time evolution of the internal structure of a star for $M_{\mathrm{He,init}} = 60\ M_\odot$ for different assumptions for the $^{12}\mathrm{C}(\alpha, \gamma)^{16}\mathrm{O}$ reaction rate. The top row shows the signed logarithm of the net specific power, i.e., $\mathrm{sign}(\epsilon_{\mathrm{nuc}} - \epsilon_\nu) \log_{10}(\max(1.0, |\epsilon_{\mathrm{nuc}} - \epsilon_\nu|)/(\mathrm{erg\ g^{-1}\ s^{-1}}))$, where ϵ_{nuc} is the specific power from nuclear reactions and ϵ_ν is the specific power lost via neutrinos. Purple regions denote strong neutrino cooling and red regions denote strong nuclear burning. Hatched regions indicate convective mixing regions. Text labels state the primary fuel burned in that region. Points marked on the top x-axis correspond to those marked in Figure 3, given with approximate timescales. The middle row shows the evolution of Γ_1 (Equation (1)), regions with $\Gamma_1 - 4/3 < 0$ are locally unstable. The bottom row shows the density-temperature structure of the inner region of the stars at the points marked in the top panel, light colors denote later phases. The dashed line shows where the gas pressure is approximately equal to the radiation pressure. The solid black line that encloses $\Gamma_1 < 4/3$ shows the approximate location of the pair-instability region.

come from alternative formation mechanisms—for instance, second-generation mergers (Rodriguez et al. 2016, 2019; Gerosa & Berti 2019), primordial black holes (Carr et al. 2016; Ali-Haïmoud et al. 2017), or accretion onto the black hole (Roupas & Kazanas 2019; Di Carlo et al. 2020a; van Son et al. 2020).

The detection of the upper edge of the PISN mass gap ($M_{\mathrm{BH}} > 120\ M_\odot$) would provide a strong constraint on the $^{12}\mathrm{C}(\alpha, \gamma)^{16}\mathrm{O}$ rate. This edge has smaller numerical uncertainties associated with it, because it is defined only by a combination of fundamental physics (nuclear reaction rates and the EOS of an ionized gas) and does not depend on the complexities of modeling the hydrodynamical pulses that define the lower edge of the PISN mass gap. Mergers in this mass range are expected to be rare due to the difficulty in producing sufficiently massive stars in close binaries (Belczynski et al. 2016a), but they may be detectable by third-generation gravitational-wave detectors (Mangiagli et al. 2019).

4.1. Other Sources of the $^{12}\mathrm{C}(\alpha, \gamma)^{16}\mathrm{O}$ Rate

Table 1 shows the maximum black hole mass as a function of different sources for the $^{12}\mathrm{C}(\alpha, \gamma)^{16}\mathrm{O}$ reaction. The `STARLIB` rate of Sallaska et al. (2013) is based on that of Kunz et al. (2002); however, `STARLIB` assumes that the rate probability density is log-normal, thus its median value is $\sqrt{R_{\mathrm{Low}} \times R_{\mathrm{High}}}$ (Equation (17) in Sallaska et al. 2013), where R_{Low} and R_{High} are from Kunz et al. (2002). The maximum black hole mass for the rate of deBoer et al. (2017) is computed using the "adopted," "lower," and "upper" rates from Table 10XV of deBoer et al. (2017). The lower edge of the black hole mass gap over the different sources is between 47 and 51 $M_\odot$, with an uncertainty on the maximum black hole mass of <5%. The upper edge varies between 130 and 136 $M_\odot$, with a similar uncertainty on the maximum black hole mass of <5%.

The small variations seen in the edges of the PISN mass gap are due to the fact that the different sources of the $^{12}\mathrm{C}(\alpha, \gamma)^{16}\mathrm{O}$ rate have been slowly converging over time on an S-factor

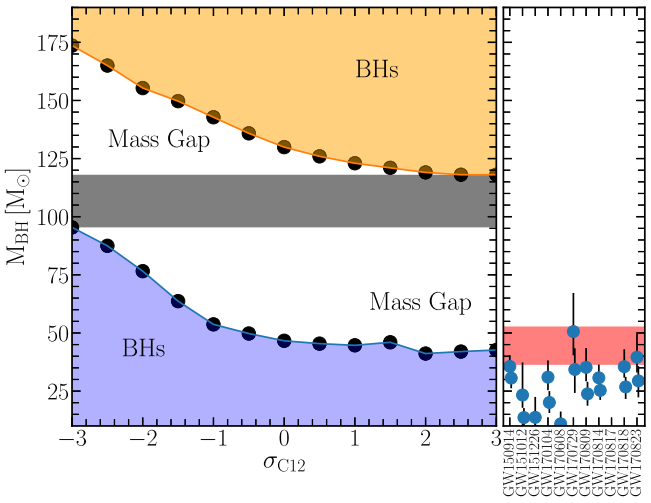

Figure 5. The location of the PISN mass gap as a function of the temperature-dependent uncertainty in the $^{12}C(\alpha, \gamma)^{16}O$ reaction rate. The white region denotes the mass gap, while the gray horizontal bar denotes the mass range where we cannot place a black hole for any value of the $^{12}C(\alpha, \gamma)^{16}O$ rate. The side plot shows the inferred masses of the currently known black holes from LIGO/Virgo O2 (Abbott et al. 2019a), with their 90% confidence intervals. The red region shows the 90% confidence range for the inferred location of the lower edge of the PISN mass gap from the O1/O2 data (Abbott et al. 2019b).

Table 1
Location of the Edges of the PISN Mass Gap for Different Sources of the $^{12}C(\alpha, \gamma)^{16}O$ Reaction Rate

Source	Lower ($M_\odot$)	Upper ($M_\odot$)
1.7 × Caughlan & Fowler (1988)	49	135
Angulo et al. (1999) (NACRE)	49	130
Kunz et al. (2002)[a]	50	134
Cyburt et al. (2010) (REACLIB)	50	136
Sallaska et al. (2013) (STARLIB)[b]	47^{+7}_{-2}	130^{+13}_{-7}
deBoer et al. (2017)[c]	51^{+0}_{-4}	134^{+5}_{-5}

Notes. Uncertainties quoted are 1σ where applicable.
[a] Based on the "adopted" fitting coefficients in Table 5 of Kunz et al. (2002).
[b] The STARLIB median rate is based on $\sqrt{R_{Low} \times R_{High}}$ (Equation (17) in Sallaska et al. 2013), where the rates R_{Low} and R_{High} come from Table 5 of Kunz et al. (2002).
[c] Based on the "adopted," "lower," and "upper" rates from Table 10XV of deBoer et al. (2017).

between 140 and 160 keV b (see Figure 7). See Figure 26 of deBoer et al. (2017) for a review of how the uncertainty in the different energy levels has improved since the 1970s.

4.2. Sensitivity to Other Reaction Rates

Table 2 shows how the maximum black hole mass varies as a function of both the $^{12}C(\alpha, \gamma)^{16}O$ rate and the rates of other reactions that either create carbon (the 3α reaction), destroy carbon ($^{12}C + {}^{12}C$), or burn oxygen ($^{16}O + {}^{16}O$). For each rate varied we compute the location of the mass gap for the number of standard deviations from the median for that rate, and for variations in the $^{12}C(\alpha, \gamma)^{16}O$ reaction. This is to probe for correlations between the rates. In the case of the rates from Caughlan & Fowler (1988) we follow the uncertainty provided by STARLIB and we multiply (divide) the rate by a fixed factor of 10 due to the lack of knowledge of the uncertainty in this rate. Table 2 then shows the fractional change in the location of each edge of the mass gap as an indication of how sensitive the edges of the mass gap are to other uncertainties. In general the maximum fractional error in the location of the PISN mass gap is ≈5%–15% from considering other reactions.

We would expect that varying a rate between its upper and lower limits would produce relative changes with opposing signs, but in some cases this does not occur. This is due to numerical difficulties in the evolution of the models. Some of these models would fail to reach core collapse, and thus we could not measure the peak of the black hole mass distribution. Instead, we report the largest black hole mass only for the models that successfully reach core collapse. This means that the relative change we measure includes changes in the initial mass as well as the black hole mass. Table 2 should therefore be taken as a representation of the changes expected for different rates, but it does not show the complete picture.

For the STARLIB median $^{12}C(\alpha, \gamma)^{16}O$ reaction rate, the 3α reaction produces a fractional uncertainty of 1%–10%, independent of the $^{12}C(\alpha, \gamma)^{16}O$ rate. By increasing the 3α rate within its 1σ uncertainties, we decrease the maximum black hole mass. There is a much larger change when reducing the rate than when increasing it.

To test variations in the $^{12}C + {}^{12}C$ rate we use the rate provided by Tumino et al. (2018), which provides a temperature-dependent 1σ uncertainty on the reaction rate. However, the uncertainty is only available up to 3 GK; at higher temperatures we revert to MESA's standard $^{12}C + {}^{12}C$ reaction rate, which does not have an uncertainty estimate provided (Caughlan & Fowler 1988).

It is difficult to determine the trend in black hole mass with the $^{12}C + {}^{12}C$ rate given that a number of models do not converge. We might expect variations around ≈15%. A larger change occurs when $\sigma_{C12} \geqslant 0$ than when $\sigma_{C12} = -3$. This is due to the change in the power generated during the carbon burning. When the $^{12}C + {}^{12}C$ rate is increased, stars with low ^{12}C fractions ($\sigma_{C12} \geqslant 0$), which would not generate a convective carbon shell (when $^{12}C + {}^{12}C$ is small), can now generate sufficient power to alter the core structure and potentially drive the formation of a convective carbon-burning shell. See, however, Tan et al. (2020) for a discussion on why the rate of Tumino et al. (2018) may have been overestimated, and Fruet et al. (2020) for a discussion on new techniques for measuring the $^{12}C + {}^{12}C$ rate.

As the $^{16}O + {}^{16}O$ rate increases, the maximum black hole mass decreases. This change is asymmetric, with a larger change occurring when the rate decreases than when it increases. The 0% change seen when $\sigma_{C12} = -3$ is due to those stars lacking pulsations. As such a star has a high ^{12}C fraction, and thus a carbon shell, it does not undergo explosive oxygen burning, just stable core oxygen burning. There are no pulsations, so no mass is lost. This rate does have an effect on the core structure of the star, which might lead to variations in the mass lost during the final collapse into a black hole. For larger values of σ_{C12} there is up to a 10% variation in the location of the edges of the PISN mass gap.

More work is needed to understand the correlations between the different reaction rates and their effect on our ability to constrain the edges of the PISN mass gap, e.g., West et al. (2013). We need to improve our understanding of how the uncertainty in the rates at different temperatures alters the behavior of the carbon shell and the final black hole mass. This could be achieved with a Monte Carlo sampling of the reaction

Table 2
Relative Change in the Location of the Upper and Lower Edges of the PISN Mass Gap, when Varying Both the $^{12}C(\alpha, \gamma)^{16}O$ Reaction Rate and Either the 3α, $^{12}C+^{12}C$, or $^{16}O+^{16}O$ Reaction Rate, with Respect to Our Default Choices

Rate	Uncertainty	$^{12}C(\alpha, \gamma)^{16}O$					
		$\sigma_{C12} = -3$		$\sigma_{C12} = 0$		$\sigma_{C12} = +3$	
		Lower	Upper	Lower	Upper	Lower	Upper
3α	$+1\sigma$	−1.0%	−2.7%	1.7%[a]	−0.8%	−4.3%[a]	−0.8%
Sallaska et al. (2013)	-1σ	6.2%	4.2%	8.9%[a]	4.6%	−7.6%[a]	0.8%
$^{12}C + {}^{12}C$	$+1\sigma$	−1.0%	0.5%[a]	16.6%	∼0.0%	−16.8%[a]	∼0.0%
Tumino et al. (2018)	-1σ	1.9%	0.5%[a]	−1.4%	∼0.0%	−1.2%[a]	∼0.0%
$^{16}O + {}^{16}O$	×10	0.0%[b]	−1.8%	0.0%	−2.3%	−2.6%	−3.3%
Caughlan & Fowler (1988)	×0.1	0.0%[b]	4.4%	5.7%	9.1%	6.9%	9.2%

Notes.
[a] Variations have the same sign because numerical difficulties prevent comparison between similar models.
[b] No variation seen because most burning occurs at temperatures where the rate has reverted to that of Caughlan & Fowler (1988) and thus shows no variation.

rates, e.g., Rauscher et al. (2016) and Fields et al. (2016, 2018), but this comes at a much greater computational cost.

5. Constraining the $^{12}C(\alpha, \gamma)^{16}O$ Reaction Rate with Gravitational Waves

Because of the sensitivity of the edges of the PISN mass gap to the $^{12}C(\alpha, \gamma)^{16}O$ reaction rate, we can use the measured location of the gap to derive a value for this rate at astrophysically relevant temperatures. See Appendix B for the sensitivity of our results to different temperature ranges. We focus here on the lower edge of the mass gap, because it has been inferred from the existing LIGO/Virgo data (Abbott et al. 2019b).

The currently most massive black hole in O1/O2, as inferred by LIGO/Virgo, is GW170729 at $M_{BH} = 50.6^{+16.6}_{-10.2}\ M_\odot$ (Abbott et al. 2019b), which could be used as an estimate for the location of the PISN mass gap, assuming that it is from a first-generation black hole. There are also several other candidates for the most massive black hole. These include IMBHC-170502, which has been inferred to have individual black hole components with masses $\approx 94\ M_\odot$ and $\approx 62\ M_\odot$ (Udall et al. 2020). GW151205 has also been proposed to have one component with an inferred mass of $M_{BH} = 68^{+28}_{-17}\ M_\odot$ (Nitz et al. 2020). By having a component mass inside the classical PISN mass gap, it was suggested that this event was the result of dynamical mergers.

However, we must be careful not to overinterpret single events, which may be susceptible to noise fluctuations (Fishbach et al. 2020), which can make a black hole have a higher apparent mass than it truly does. For instance, considering GW170729 jointly with the other O1/O2 detections lowers its mass to $M_{BH} = 38.9^{+7.3}_{-4.5}\ M_\odot$, which places it below the PISN mass gap.

Thus we must consider the entire population of BBH mergers as a whole when measuring the maximum inferred black hole mass below the gap. The 10 detections in O1/O2 place the maximum black hole mass below the PISN mass gap at 42–44 $M_\odot$ depending on the choice of model parameters (Abbott et al. 2019b). The current 90% confidence interval on this value is $\approx \pm 10\ M_\odot$. With a large enough population ($\mathcal{O}(50)$) of black holes we can place limits of $\approx \pm 1\ M_\odot$ on the location of the gap (Fishbach & Holz 2017; Abbott et al. 2019b).

We assume that all BBH mergers so far detected come from isolated binaries or first-generation black hole mergers, thus the maximum-mass black holes below the gap come from PPISNe. We also assume that only uncertainties in $^{12}C(\alpha, \gamma)^{16}O$ matter. Thus we can use the posterior distribution over the maximum black hole mass for the population of black holes as the estimate of the maximum black hole mass below the mass gap.

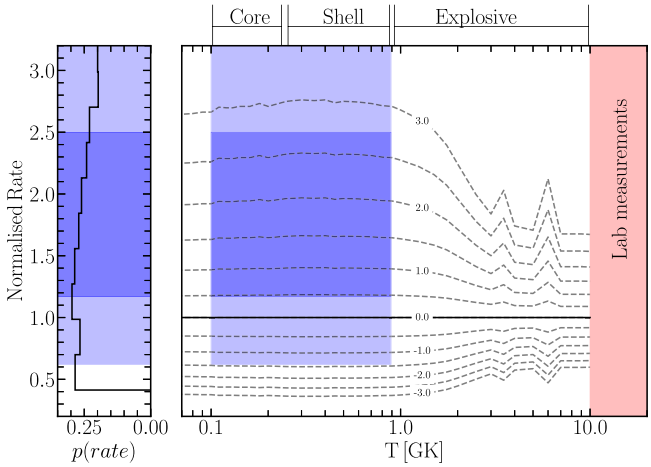

Figure 6. The right panel shows the $^{12}C(\alpha, \gamma)^{16}O$ rate as a function of temperature, normalized to the median STARLIB rate $\langle\sigma\nu\rangle/\langle\sigma\nu\rangle_{median} = e^{\mu(T)\sigma_{C12}}$. The left panel shows the posterior of our distribution. The solid line, labeled 0.0, indicates the normalized median rate (i.e., $\sigma_{C12} = 0.0$). The dashed lines show the reaction rates above and below the median STARLIB rate, labeled by the appropriate value of σ_{C12}. We assume that the black hole mass distribution is given by model B of Abbott et al. (2019b). The dark blue region shows the 50% confidence range in the $^{12}C(\alpha, \gamma)^{16}O$ rate, while the lighter blue shows the 90% confidence interval. Note the upper rate limit is unbounded when adopting the current O2 LIGO/Virgo posteriors on the maximum black hole mass. The red region ($T > 10$ GK) shows the approximate lower edge of the energy range for lab measurements of the $^{12}C(\alpha, \gamma)^{16}O$ rate (Holt et al. 2019).

Figure 6 shows the uncertainty in the STARLIB $^{12}C(\alpha, \gamma)^{16}O$ reaction rate as a function of temperature. Over the temperatures we are sensitive to—less than 1.0 GK, where helium burns non-explosively—the uncertainty is approximately constant. Thus we need only find a single temperature-independent σ_{C12} to fit to the maximum black hole mass below the gap.

We fit a fourth-order polynomial to the lower edge of the PISN mass gap (Figure 5) to map from maximum black hole mass to σ_{C12}. This is then combined with the posterior of the maximum black hole mass to generate a posterior distribution

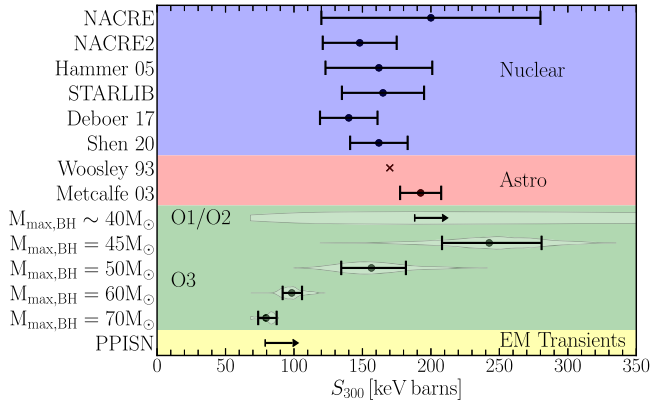

Figure 7. Constraints on the S-factor at 300 keV for the $^{12}C(\alpha, \gamma)^{16}O$ reaction rate. The blue region presents values for commonly used nuclear reaction rate libraries, while the red region shows values inferred from astrophysical measurements, by observations of white dwarfs (Metcalfe 2003), and from the galactic chemical enrichment model of Woosley et al. (1993). The green region show our posteriors on the $^{12}C(\alpha, \gamma)^{16}O$ derived from the O1/O2 maximum black hole mass inferred from model B of Abbott et al. (2019b), and for 50 simulated observations of binary black holes, approximately the number expected in O3, assuming that the O3 detections follow the power-law model B from Abbott et al. (2019b). Error bars show the 68% confidence intervals on our inferred S-factor at 300 keV. The yellow region shows the constraints placed if PPISNe exist (Section 7.2). Error bars in the blue and red regions are 1σ uncertainties. We assume that the uncertainty from Shen et al. (2020) is the same as that of deBoer et al. (2017).

over σ_{C12}. The blue boxes in Figure 6 show our 50% and 90% confidence interval on σ_{C12}. At 50% confidence, we can limit σ_{C12} to be between 0.5 and 2.5, while at 90% confidence we can only place a lower limit of $\sigma_{C12} > -1.5$. This is due to the posterior distribution from LIGO/Virgo allowing the maximum black hole mass to be $M_{BH,max} < 40\ M_\odot$, which is below the lower limit we find for the edge of the mass gap.

By taking the STARLIB astrophysical S-factor, at 300 keV, to be 165 keV b (Sallaska et al. 2013) we can scale the S-factor from σ_{C12}. As the normalized rate is approximately flat (Figure 6) the uncertainty is flat. Using Equation (4) and Figure 6, we have $e^{\mu(T)\sigma_{C12}} = \langle\sigma\nu\rangle / \langle\sigma\nu\rangle_{median} \propto S(300\ keV)$, thus the S-factor can be linearly scaled from its STARLIB value to a new value, given by a different σ_{C12}.

Figure 7 shows a comparison between the values for the S-factor from nuclear laboratory experiments, constraints placed by white dwarf asteroseismology and models of galactic chemical enrichment, and this study. For our assumptions we find the S-factor for the $^{12}C(\alpha, \gamma)^{16}O$ rate at 300 keV to be $S_{300} > 175$ keV b at 68% confidence. At 95% confidence we find a limit of $S_{300} > 82$ keV b and at 99% confidence we find a limit of $S_{300} > 68$ keV b. The S-factors computed here are consistent with experimentally derived values, though we only currently place a lower limit on the S-factor. See Section 6 for a discussion on how this limit may be improved with future gravitational-wave detections. Figure 7 also shows the lower limit on the S-factor if PPISNe can be shown to exist through other means, for instance electromagnetic observations of the SN. The existence of PPISN would imply that $S_{300} > 79$ keV b; this is discussed further in Section 7.2.

5.1. GW190521

The detection of GW190521 (Abbott et al. 2020a) with component masses of $85^{+21}_{-14}\ M_\odot$ and $66^{+17}_{-18}\ M_\odot$ places *both* black holes firmly in the mass gap, as inferred from the O1/O2 observations (Abbott et al. 2020b). However, if we assume that the primary black hole in GW190521 was a first-generation black hole, this leads to an inference of $\sigma_{C12} = -2.4^{+0.6}$, and thus $S(300\ keV) = 73^{+11}$ keV b. We cannot infer a lower limit because the 90% confidence interval for the mass extends above $M_{BH} \approx 95\ M_\odot$, where our models cannot place a black hole, below the mass gap. If $\sigma_{C12} \approx -2.5$, then PPISNe would be suppressed by the carbon-burning shell. Instead, if we assume that only the secondary object was a first-generation black hole we would infer $\sigma_{C12} = -1.7^{+1.8}_{-0.5}$, and thus $S(300\ keV) = 87^{+84}_{-12}$ keV b.

However, it is unlikely that GW190521 is a pair of first-generation black holes; instead it is likely to be a pair of second-generation black holes, perhaps inside the disk of an active galactic nucleus (AGN) (Abbott et al. 2020b). Indeed, Graham et al. (2020) claims a tentative detection of an electromagnetic counterpart (ZTF19abanrhr) due to the merger product ramming into an AGN disk. However, the redshift of the AGN does not agree with the GW-inferred redshift. Further investigation of this event and the likelihood of a double second-generation merger in an AGN disk is warranted. The presence of black holes in the expected mass gap can make the analysis of the location of the gap more difficult, though folding in a prior based on the $^{12}C(\alpha, \gamma)^{16}O$ rate may help to identify outliers that have formed through alternative formation mechanisms.

6. Prospects for Constraining $^{12}C(\alpha, \gamma)^{16}O$ from Future GW Detections

With the release of the O3 data from LIGO/Virgo, it is predicted that there will be $\mathcal{O}(50)$ BBH detections (Abbott et al. 2018). Thus we can ask how well can we expect to do with additional observations? This depends strongly on what value the lower edge of the PISN mass gap is found to have.

We assume that the detections in O3 will follow a power law in primary mass (M_1) of the black hole in the binary, with the form previously assumed for the O1/O2 data (Abbott et al. 2019b). Thus we have

$$p(M_1) \propto M_1^{\alpha} \tag{7}$$

for $M_{min} < M_1 < M_{max}$, where M_{min} is the minimum possible black hole mass below the PISN mass gap, and M_{max} is the maximum possible black hole mass. We also assume that the secondary mass M_2 follows

$$p(M_2|M_1) \propto M_2^{\beta} \tag{8}$$

where $M_{min} < M_2 < M_1$. This is equivalent to model B of Abbott et al. (2019b). We set $M_{min} = 5\ M_\odot$ and $\beta = 4$ to be consistent with the current O1/O2 observations (Abbott et al. 2019b). There is a strong correlation between the values of α and M_{max}. Thus for different choices of M_{max} we choose a value of α that remains consistent with the O1/O2 data (e.g., Figure 3 of Abbott et al. 2019b). As M_{max} increases, we require a larger α value. We consider four possible locations for the lower edge of the PISN mass gap (M_{max}) to explore how the uncertainty both from the LIGO/Virgo measurements and from our stellar models affects our determination of the $^{12}C(\alpha, \gamma)^{16}O$ rate. We considered $M_{max} = 45, 50, 60, 70\ M_\odot$, and we choose $\alpha = -1.5, -1.5, -2, -3$, to remain consistent with the joint α, M_{max} posterior from O1/O2 (Abbott et al. 2019b).

We generate 50 mock detections from each of the four mass distributions described above. We assume that the underlying merger rate density is constant in redshift, and that sources are detected if they pass a signal-to-noise ratio threshold of 8 in a single detector. We neglect the spins of the black holes in this study, because the maximum mass is well measured independently of the underlying spin distribution. For each mock detection, we simulate the measurement uncertainty on the source-frame masses according to the prescription in Fishbach et al. (2020), which is calibrated to the simulation study of Vitale et al. (2017). This gives a typical 1σ measurement uncertainty of $\sim$30% on the source-frame masses. We then perform a hierarchical Bayesian analysis (Mandel 2010; Mandel et al. 2019) on each set of 50 detections to recover the posterior over the population parameters, α, $M_{\rm max}$, β, and $M_{\rm min}$. This provides a projection of how well $M_{\rm max}$, the maximum mass below the PISN mass gap, can be measured with 50 observations. We sample from the hierarchical Bayesian likelihood using `PyMC3` (Salvatier et al. 2016). Finally, we translate the projected measurement of $M_{\rm max}$ under each of the simulated populations to a measurement of the ^{12}C(α, γ)^{16}O reaction rate according to Figure 5.

Figure 7 shows our inferred S-factors (at 300 keV) for different choices of the maximum black hole mass below the PISN mass gap. As the maximum black hole mass increases, the S-factor decreases (as stars have more ^{12}C in their core and thus have reduced mass loss from pulsations). The 68% confidence interval also reduces in size as the maximum black hole mass increases. The predicted accuracy with which LIGO/Virgo is expected to infer the maximum black hole mass decreases as the mass increases, because we require a steeper power-law index α to be consistent with the O1/O2 observations. This leads to fewer mergers near the gap. However, the maximum black hole mass becomes more sensitive to the choice of $\sigma_{\rm C12}$. This can be seen in the gradient of the lower edge of the PISN mass gap in Figure 5, which increases as $\sigma_{\rm C12}$ decreases. We caution that we have likely underestimated the size of the uncertainty range, especially at the higher black hole masses, due to the effect of uncertainties in other reaction rates and mass lost during the formation of the black hole. With the predicted accuracy expected for LIGO/Virgo during O3 in inferring the maximum black hole mass, we will be limited by the accuracy of our models, not the data, in constraining the ^{12}C(α, γ)^{16}O reaction rate.

7. Other Observables

7.1. Formation Rates

The initial mass function (IMF) strongly favors less massive progenitors, which implies that PPISNe and PISNe should be more common at higher values of $\sigma_{\rm C12}$ (higher ^{12}C(α, γ)^{16}O rates), all else being equal. This is potentially detectable given a sufficiently large population of BBH mergers or PPISN/PISN transients, and could provide additional constraints on the ^{12}C(α, γ)^{16}O rate. A number of upcoming surveys, including `LSST`, `JWST`, and `WFIRST`, are expected to find significant numbers of PPISN and PISN transients (Young et al. 2008; Hummel et al. 2012; Whalen et al. 2013a, 2013b; Villar et al. 2018; Regős et al. 2020).

To provide a rough estimate for this, we make the simplified assumption that the helium core masses follow a Salpeter-like IMF with a power law $\alpha = -2.35$, so that we can compare the relative difference in formation rates for stars with $\sigma_{\rm C12} = \pm 1$. We take the smallest helium cores to be $M_{\rm He,init} = 30\,M_\odot$ (the least massive stars modeled in our grid), and the maximum helium core mass that makes a black hole to be $73\,M_\odot$ for $\sigma_{\rm C12} = -1$, and $61\,M_\odot$ for $\sigma_{\rm C12} = +1$. This folds together the formation rates of black holes from both core collapse and PPISNe, because these objects cannot be distinguish from their gravitational-wave signals alone. This leads to a relative increase in the formation rate of black holes of $\approx$10% for models with $\sigma_{\rm C12} = -1$ over those with $\sigma_{\rm C12} = +1$. A larger variation is possible if we consider how the lowest-mass helium core that makes a black hole varies with ^{12}C(α, γ)^{16}O. $\sigma_{\rm C12} = \pm 1$ puts the lower limit at $5\,M_\odot$ and $8\,M_\odot$ (Sukhbold & Adams 2020), which would lead to a factor of 2 difference in the formation rates of black holes. This is mostly due to the change in the relative number of low-mass black holes.

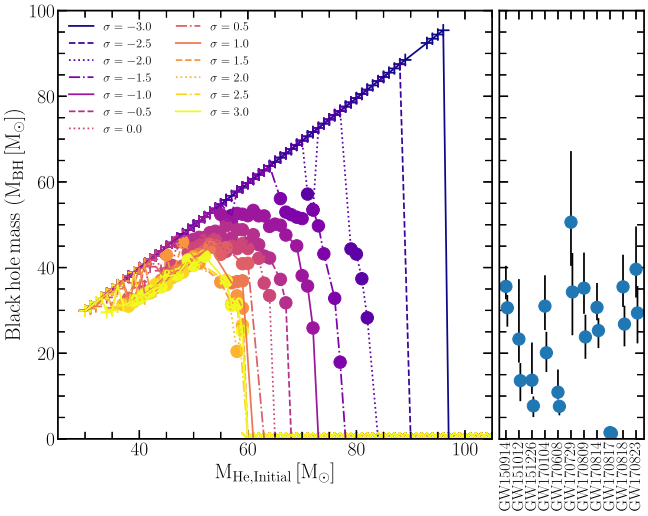

Figure 8. The final black hole mass as a function of the initial helium core mass. The colors represent different choices for $\sigma_{\rm C12}$. Circles denote models that undergo pulsational mass loss (PPISN), while plus symbols denote models that do not undergo mass loss due to pulsations (CC). The right panel shows the inferred masses of the currently known black holes from LIGO/Virgo O2 (Abbott et al. 2019a), with their 90% confidence intervals.

Figure 8 shows the black hole masses as a function of the initial helium core mass for different choices of $\sigma_{\rm C12}$. At the lowest values of $\sigma_{\rm C12}$, no star undergoes PPISN, thus the black hole mass scales linearly with the initial helium core mass. As $\sigma_{\rm C12}$ increases, the final black hole mass shifts to lower masses away from a linear relationship with the helium core mass, due to pulsational mass loss. There is also a turnover in the initial black hole mass relationship, where the most massive black holes do not form from the most massive stars undergoing PPISNe (Farmer et al. 2019). This turnover may be detectable in the inferred black hole mass distribution (see model C of Abbott et al. 2019b). There may also be a small bump in the black hole mass distribution at the interface between the stars undergoing CC and the lightest PPISN progenitors, depending on the strength of the mass loss in the latter (Renzo et al. 2020b). We chose not to show Figure 8 in terms of the carbon core mass, which is the more applicable quantity to show when comparing between different metallicities (Farmer et al. 2019), because the highest $\sigma_{\rm C12}$ models have $X(^{12}{\rm C}) \approx 0$ in their cores. This leads to the carbon core mass being ill-defined.

We can compare the formation rates of PPISNe (and thus potentially detectable supernovae) only for $\sigma_{\rm C12} > -2.0$. As an

indication of the variation, we consider the relative change (due to the IMF) in formation rates only for $\sigma_{C12} = \pm 1$. We find the helium core masses for stars that we would classify as undergoing a PPISN to be 41–61 $M_\odot$ for $\sigma_{C12} = +1$ and 55–73 $M_\odot$ for $\sigma_{C12} = -1$. This leads to an increase by a factor of 2 for $\sigma_{C12} = +1$ over $\sigma_{C12} = -1$. However, there can be difficulty in determining which stars are PPISNe due to the small amounts of mass lost for the lightest PPISN progenitors (Renzo et al. 2020a).

For the rate of PISNe, we find the initial helium core masses to be 61–124 $M_\odot$ for $\sigma_{C12} = +1$ and 73–142 $M_\odot$ for $\sigma_{C12} = -1$. These ranges then lead to a relative increase of ≈30% for the rate of PISNe for $\sigma_{C12} = +1$ compared to $\sigma_{C12} = -1$. These variations are driven by the change in the lower masses needed for a PPISN or PISN as the $^{12}C(\alpha, \gamma)^{16}O$ rate increases (Takahashi 2018).

7.2. Observations of Supernovae

In Figure 1 we show that no PPISNe are formed when $\sigma_{C12} < -2$. This provides an intriguing observational test for the $^{12}C(\alpha, \gamma)^{16}O$ reaction rate. If the existence of PPISNe can be confirmed though photometric observations (for instance, candidate PPISN SN 2006gy (Woosley et al. 2007), SN 2006jc (Pastorello et al. 2007), SN iPTF14hls (Arcavi et al. 2017; Woosley 2018; Vigna-Gómez et al. 2019), SN iPTF16eh (Lunnan et al. 2018), SN 2016iet (Gomez et al. 2019), or SN 2016aps (Nicholl et al. 2020)) then we can place a lower limit on the $^{12}C(\alpha, \gamma)^{16}O$ reaction rate of $\sigma_{C12} > -2.0$.

The outer layers of the star that are expelled in a pulsational mass loss event, or even the small amount of material that might be ejected in the final collapse to a black hole, provides some information on the final composition of the star, though this will depend on the star's metallicity and assumed wind mass loss rate. In general the least massive stars that undergo a PPISN, in our grid, have surface layers dominated by ^{4}He, while the more massive stars have ^{16}O-rich outer layers (Renzo et al. 2020a).

As the initial mass increases, and the pulses get stronger and thus remove more mass, they can expose ^{16}O-rich layers, with traces of ^{20}Ne, ^{23}Na, ^{24}Mg, and ^{28}Si (Renzo et al. 2020a). However, the ^{12}C fraction in the outer layers follows the same trend seen in the core ^{12}C fraction. As the $^{12}C(\alpha, \gamma)^{16}O$ reaction rate increases, more ^{12}C is converted into ^{16}O in helium shell burning. Therefore, the measured abundances could provide additional constraints on $^{12}C(\alpha, \gamma)^{16}O$, and may provide constraints in a reduced temperature region (that associated with helium shell burning, $0.3 < T/\mathrm{GK} < 1.0$). Further work is needed to quantify the amount of mixing in the outer layers of the star (Renzo et al. 2020b), to understand which parts of the ejecta (and thus which layers of the star) would be measured in spectroscopy of a PPISN (Renzo et al. 2020a), and to investigate the effect of a larger nuclear network in order to follow in greater detail the nucleosynthetic yields from the explosive oxygen burning (Weaver & Woosley 1993; Heger & Woosley 2002; Woosley & Heger 2007; West et al. 2013).

8. Discussion

This work assumes that all black holes found by LIGO/Virgo so far have come from stars that lose their hydrogen envelope before they collapse to a black hole. Thus the maximum mass a black hole can have is limited by PISNe and mass loss from PPISNe. However, there are formation mechanisms that may place a black hole in the mass gap. If a star can retain its hydrogen envelope until collapse, through a combination of weak stellar winds (Woosley 2017) or for a stellar merger (Spera et al. 2019; Vigna-Gómez et al. 2019), then we could find black holes up to ∼60 $M_\odot$; see van Son et al. (2020) for an overview. Black holes formed in dense stellar clusters or AGN disks (McKernan et al. 2018) can merge multiple times (Rodriguez et al. 2016; Stone et al. 2017; Di Carlo et al. 2019; Yang et al. 2019).

The first-generation black holes in these environments will be limited by the PISN mass gap, but higher generation mergers would not be limited and could populate the gap (Di Carlo et al. 2020b). Their effect on the inference of $^{12}C(\alpha, \gamma)^{16}O$ will depend on whether the kick received by the resulting black hole is small enough that the black hole stays in the cluster (Fragione & Kocsis 2018; Rodriguez et al. 2018), and thus on their uncertain contribution to the total rate of black hole mergers. If they are distinguishable from mergers due to isolated binary evolution, for instance via their spin (Fishbach et al. 2017; Gerosa & Berti 2017; Bouffanais et al. 2019; Arca Sedda et al. 2020), then they could be removed from the population used to infer the $^{12}C(\alpha, \gamma)^{16}O$ rate. It may also be possible to fit the maximum black hole mass below the gap assuming the population contains both isolated binaries and hierarchical mergers without needing to subtract the hierarchical mergers (Kimball et al. 2020) Also, if a channel that produces black holes in the mass gap is rare, we may still be able to determine the location of the mass gap for the more dominant channel.

In this work we have considered the rates of four reactions: 3α, $^{12}C(\alpha, \gamma)^{16}O$, $^{12}C + {}^{12}C$, and $^{16}O + {}^{16}O$. There are many other reaction rates that can alter the evolution of a star (Rauscher et al. 2016; Fields et al. 2018). We expect their effect to be small for the final black hole mass, compared with the reaction rates considered here, though they would play a role in the nucleosynthetic yields from the PPISN and PISN ejecta. In Farmer et al. (2019) we investigated other uncertainties, e.g., mass loss, metallicity, convective mixing, and neutrino physics, which have only a small effect of ≈10% on the location of the mass gap. How convection is treated in this hydrodynamical regime can have a small impact on the final black hole mass for stars at the boundary between core collapse and PPISN, i.e., where the pulses are weak. However, the edge of the PISN mass gap is not affected, because the pulses experienced by a star near the mass gap are stronger (Renzo et al. 2020b). In this work we considered only non-rotating models. Rotation may play a role in the final black hole mass, depending on how material with high angular momentum is accreted onto the black hole during the collapse (Fryer & Warren 2004; Rockefeller et al. 2006; Batta et al. 2017).

By assuming that the entire bound mass of the star collapses into a black hole, we place an upper limit on the black hole mass possible for a PPISN. If the star were to lose mass during the collapse, then we would overestimate the inferred S-factor for the $^{12}C(\alpha, \gamma)^{16}O$ reaction rate. If the star forms a proto-neutron star during its collapse it might eject ≈10% of the proto-neutron star mass as neutrinos, ≈0.1 $M_\odot$ (Fryer 1999; Fryer et al. 2012). The envelope of the star may then respond to the change in the gravitational potential, generating a weak shock that unbinds material with binding energies less than 10^{47} erg (Nadezhin 1980; Lovegrove & Woosley 2013; Fernández et al. 2018). However,

stars undergoing a PPISN will have already expelled their weakly bound outer envelopes, thus mass lost via a weak shock is limited to a few tenths of a solar mass. If a jet is produced, by accretion onto the compact object, then there may be an ejection of $>1\,M_{\odot}$ of material (Gilkis et al. 2016; Quataert et al. 2019). If we assume $1\,M_{\odot}$ of mass loss during the collapse, then our inferred S-factor at 68% confidence decreases from $S_{300} > 175$ keV b to $S_{300} > 159$ keV b. Further work is needed to understand the collapse mechanism of these massive cores, and whether we can extrapolate from models of stars that collapse with cores of 5–10 $M_{\odot}$ to those with cores of $\approx 50\,M_{\odot}$.

Previous studies of PPISN and PISN progenitors have found the location of the PISN mass gap consistent with ours, 50–53 $M_{\odot}$ (Yoshida et al. 2016), $\approx 48\,M_{\odot}$ (Woosley 2017), $\approx 50\,M_{\odot}$ (Leung et al. 2019). The small variations in the location of the gap can be attributed to differences in chosen metallicity, mass loss rates, and source of the $^{12}\mathrm{C}(\alpha, \gamma)^{16}\mathrm{O}$ reaction rate. Takahashi (2018) showed how increasing the reaction rate decreases the initial mass needed for a PISN, in agreement with our findings and that the range of initial masses that can form a PPISN is reduced as the reaction rate decreases.

9. Summary

With the rapid increase in the number of gravitational-wave detections, the hope is that they can be used to start drawing lessons about the uncertain physics of their massive-star progenitors. In an earlier paper (Farmer et al. 2019) we speculated that measurements of the edge of the predicted black hole mass gap due to pair instability could be used to constrain the nuclear reaction rate of carbon capturing alpha particles and producing oxygen ($^{12}\mathrm{C}(\alpha, \gamma)^{16}\mathrm{O}$). This reaction rate is very uncertain but has large astrophysical significance. It is crucial in determining the final properties and fate of a star, and as we explicitly show in this work, the predictions for the location of the pair-instability mass gap.

We show that the physical reason why this reaction rate is so important is that it determines the relative fractions of carbon and oxygen in the core at the end of helium burning. In models for which we adopted a lower reaction rate, enough carbon is left to ignite such that it effectively delays the ignition of oxygen. As carbon–carbon burning occurs in a shell, the core inside the shell contracts to higher densities. This increases the effects of electron degeneracy and gas pressure, which stabilize the core. The formation of electron–positron pairs is then suppressed due to the increased occupation fraction of the low-energy states for electrons. Oxygen can then ignite stably even for higher core masses.

In contrast, in models for which we assume higher reaction rates, almost all carbon is depleted at the end of helium burning. The star then skips carbon–carbon burning and oxygen ignites explosively. The net effect is that increasing the $^{12}\mathrm{C}(\alpha, \gamma)^{16}\mathrm{O}$ reaction rate pushes the mass regime for pair pulsations and pair-instability supernovae to lower masses. This allows for lower-mass black holes and thus shifts the location of the pair-instability mass gap to lower masses.

Our results can be summarized as follows.

1. The location of the gap is sensitive to the reaction rate for alpha captures onto carbon, but the width of the mass gap is not. The mass gap varies between $47^{+49}_{-4}\,M_{\odot}$ for the lower edge and $130^{+44}_{-12}\,M_{\odot}$ for the upper edge, for $\pm 3\sigma$ variations in the $^{12}\mathrm{C}(\alpha, \gamma)^{16}\mathrm{O}$ reaction rate. The width is $83^{+5}_{-8}\,M_{\odot}$ (Figure 5).
2. We can place a lower limit on the $^{12}\mathrm{C}(\alpha, \gamma)^{16}\mathrm{O}$ reaction rate using the first 10 gravitational-wave detections of black holes. Considering only variations in this reaction, we constrain the astrophysical S-factor, which is a measure of the strength of the reaction rate, to $S_{300} > 175$ keV b at 68% confidence (Figure 7).
3. With $\mathcal{O}(50)$ detections, as expected after the completion of the third observing run, we expect to place constraints of ± 10–30 keV b on the $^{12}\mathrm{C}(\alpha, \gamma)^{16}\mathrm{O}$ S-factor. We show how the constraints depend on the actual location of the gap (Figure 7).
4. We find other stellar model uncertainties to be subdominant, although this needs to be explored further. Variations in other nuclear reactions such as helium burning (3α), carbon burning ($^{12}\mathrm{C} + {}^{12}\mathrm{C}$), and oxygen burning ($^{16}\mathrm{O} + {}^{16}\mathrm{O}$) contribute uncertainties of the order of 10% to the edge of the mass gap (Table 2). See Farmer et al. (2019) and Renzo et al. (2020b) for a discussion of the effect of physical uncertainties and numerics.
5. The unambiguous detection of pulsational pair-instability supernovae in electromagnetic transient surveys would place an independent constraint on the $^{12}\mathrm{C}(\alpha, \gamma)^{16}\mathrm{O}$ reaction rate. For the lowest adopted reaction rates ($<-2\sigma$) we no longer see pulsations due to pair instability. The detection of pulsational pair instability would thus imply a lower limit of $S_{300} > 79$ keV b for the $^{12}\mathrm{C}(\alpha, \gamma)^{16}\mathrm{O}$ reaction rate (Figure 1, Section 7.2). This will be of interest for automated wide-field transient searches such as the Legacy Survey of Space and Time (LSST).
6. Constraining nuclear stellar astrophysics is an interesting science case for third-generation gravitational-wave detectors. Future detectors such as the Einstein Telescope and Cosmic Explorer will be able to probe detailed features in the black hole mass distribution as a function of redshift, and potentially lead to detections above the mass gap. Improved progenitor models will be needed to maximize the science return as the observational constraints improve, but the future is promising.

We acknowledge helpful discussions with B. Paxton, F. Timmes, P. Marchant, E. C. Laplace, and L. van Son. R.F. is supported by the Netherlands Organization for Scientific Research (NWO) through a top module 2 grant with project number 614.001.501 (PI: de Mink). S.E.d.M. acknowledges funding by the European Union's Horizon 2020 research and innovation program from the European Research Council (ERC) (grant agreement No. 715063), and by the Netherlands Organization for Scientific Research (NWO) as part of the Vidi research program BinWaves with project number 639.042.728. S.E.d.M. also acknowledges the black hole Initiative at Harvard University, which is funded by grants from the John Templeton Foundation and the Gordon and Betty Moore Foundation to Harvard University. This work was also supported by the Cost Action Program ChETEC CA16117. This work was carried out on the Dutch national e-infrastructure with the support of SURF Cooperative. This research has made use of NASA's Astrophysics Data System.

Software: `mesaPlot` (Farmer 2018), `mesaSDK` (Townsend 2019), `ipython/jupyter` (Pérez & Granger 2007; Kluyver et al. 2016), `matplotlib` (Hunter 2007), `NumPy` (van der Walt et al. 2011), `PyMC3` (Salvatier et al. 2016), `MESA`

(Paxton et al. 2011, 2013, 2015, 2018, 2019), and pyMesa (Farmer & Bauer 2018).

Appendix A
MESA

When solving the stellar structure equations MESA uses a set of input microphysics. This includes thermal neutrino energy losses from the fitting formula of Itoh et al. (1996). The EOS is a blend of the OPAL (Rogers & Nayfonov 2002), SCVH (Saumon et al. 1995), PTEH (Pols et al. 1995), HELM (Timmes & Swesty 2000), and PC (Potekhin & Chabrier 2010) EOSs. Radiative opacities are primarily drawn from OPAL (Iglesias & Rogers 1993, 1996), with low-temperature data from Ferguson et al. (2005) and the high-temperature, Compton scattering-dominated regime from Buchler & Yueh (1976). Electron conduction opacities are taken from Cassisi et al. (2007).

MESA's default nuclear reaction rates come from a combination of NACRE (Angulo et al. 1999) and REACLIB (Cyburt et al. 2010) (*default* snapshot[7]). The MESA nuclear screening corrections are provided by Chugunov et al. (2007). Weak reaction rates are based on the following tabulations: Langanke & Martínez-Pinedo (2000), Oda et al. (1994), and Fuller et al. (1985).

Reverse nuclear reaction rates are computed from detailed balance based on the NACRE/REACLIB reaction rate, instead of consistently from the STARLIB rate. This is due to limitations in MESA. However, for the rates we are interested in—3α, $^{12}C(\alpha, \gamma)^{16}O$, $^{12}C + {}^{12}C$, and $^{16}O + {}^{16}O$—their reverse reactions have negligible impact on the star's evolution. The nuclear partition functions used to calculate the inverse rates are taken from Rauscher & Thielemann (2000).

We treat wind mass loss rates as in Marchant et al. (2019), where we assume the mass loss rate of Hamann et al. (1982, 1995) and Hamann & Koesterke (1998) with a wind efficiency of 0.1 to account for wind clumpiness. For further discussion of the effect of wind mass loss, see Farmer et al. (2019).

Appendix B
Calibration of $^{12}C(\alpha, \gamma)^{16}O$ Reaction Rate

To test which temperature range we are most sensitive to, we ran models where we used the STARLIB median $^{12}C(\alpha, \gamma)^{16}O$ rate, but changed the rate in one of three temperature regions to that of the -3σ value (for that temperature region only). These temperatures were chosen based on the type of helium burning encountered at that temperature: core helium burning $0.1 < T/\,\mathrm{GK} < 0.3$, helium shell burning $0.3 < T/\,\mathrm{GK} < 1.0$, and explosive helium burning $T > 1$ GK. For the default case of the median σ_{C12}, the maximum black hole mass was 46 $M_\odot$, and for $\sigma_{C12} = -3$ (over the whole temperature range) it was 95 $M_\odot$. When only changing the rate during the core helium burning, the maximum black hole mass became 79 $M_\odot$, for helium shell burning it was 55 $M_\odot$, and for explosive helium burning it was 46 $M_\odot$. Thus we are most sensitive to changes in the $^{12}C(\alpha, \gamma)^{16}O$ rate in the temperature range for core helium burning, with a smaller dependence on the helium shell burning region, and we are not sensitive to changes in the $^{12}C(\alpha, \gamma)^{16}O$ reaction rate in the temperature range for explosive helium burning.

[7] Dated 2017 October 20. Available from http://reaclib.jinaweb.org/library.php?action=viewsnapshots.

The changes in the maximum black hole mass occur due to the changes in the carbon fraction and where those changes occur. Changes during core helium burning primarily affect the core carbon fraction (see Section 3). The maximum black hole mass does not mass depend on the $^{12}C(\alpha, \gamma)^{16}O$ rate in the explosive helium burning regime, because no helium-rich region reaches $T > 1$ GK.

ORCID iDs

R. Farmer https://orcid.org/0000-0003-3441-7624
M. Renzo https://orcid.org/0000-0002-6718-9472
S. E. de Mink https://orcid.org/0000-0001-9336-2825
M. Fishbach https://orcid.org/0000-0002-1980-5293
S. Justham https://orcid.org/0000-0001-7969-1569

References

Abbott, B. P., Abbott, R., Abbott, T. D., et al. 2018, LRR, 21, 3
Abbott, B. P., Abbott, R., Abbott, T. D., et al. 2019a, PhRvX, 9, 031040
Abbott, B. P., Abbott, R., Abbott, T. D., et al. 2019b, ApJL, 882, L24
Abbott, R., Abbott, T. D., Abraham, S., et al. 2020a, PhRvL, 125, 101102
Abbott, R., Abbott, T. D., Abraham, S., et al. 2020b, ApJL, 900, L13
Acernese, F., Agathos, M., Agatsuma, K., et al. 2015, CQGra, 32, 024001
Ali-Haïmoud, Y., Kovetz, E. D., & Kamionkowski, M. 2017, PhRvD, 96, 123523
An, Z.-D., Chen, Z.-P., Ma, Y.-G., et al. 2015, PhRvC, 92, 045802
An, Z.-D., Ma, Y.-G., Fan, G.-T., et al. 2016, ApJL, 817, L5
Angulo, C., Arnould, M., Rayet, M., et al. 1999, NuPhA, 656, 3
Arca Sedda, M., Mapelli, M., Spera, M., Benacquista, M., & Giacobbo, N. 2020, ApJ, 894, 133
Arcavi, I., Hosseinzadeh, G., Howell, D. A., et al. 2017, Natur, 551, 64
Arnett, W. D., & Truran, J. W. 1969, ApJ, 157, 339
Barkat, Z., Rakavy, G., & Sack, N. 1967, PhRvL, 18, 379
Batta, A., Ramirez-Ruiz, E., & Fryer, C. 2017, ApJL, 846, L15
Belczynski, K., Heger, A., Gladysz, W., et al. 2016a, A&A, 594, A97
Belczynski, K., Holz, D. E., Bulik, T., & O'Shaughnessy, R. 2016b, Natur, 534, 512
Bemmerer, D., Cowan, T. E., Grieger, M., et al. 2018, EPJWC, 178, 01008
Bond, J. R., Arnett, W. D., & Carr, B. J. 1984, ApJ, 280, 825
Boothroyd, A. I., & Sackmann, I. J. 1988, ApJ, 328, 653
Bouffanais, Y., Mapelli, M., Gerosa, D., et al. 2019, ApJ, 886, 25
Brown, G. E., Heger, A., Langer, N., et al. 2001, NewA, 6, 457
Buchler, J. R., & Yueh, W. R. 1976, ApJ, 210, 440
Burbidge, E. M., Burbidge, G. R., Fowler, W. A., & Hoyle, F. 1957, RvMP, 29, 547
Carr, B., Kühnel, F., & Sandstad, M. 2016, PhRvD, 94, 083504
Cassisi, S., Potekhin, A. Y., Pietrinferni, A., Catelan, M., & Salaris, M. 2007, ApJ, 661, 1094
Caughlan, G. R., & Fowler, W. A. 1988, ADNDT, 40, 283
Chen, K.-J., Woosley, S., Heger, A., Almgren, A., & Whalen, D. J. 2014, ApJ, 792, 28
Chugunov, A. I., Dewitt, H. E., & Yakovlev, D. G. 2007, PhRvD, 76, 025028
Cyburt, R. H., Amthor, A. M., Ferguson, R., et al. 2010, ApJS, 189, 240
de Mink, S. E., & Mandel, I. 2016, MNRAS, 460, 3545
deBoer, R. J., Görres, J., Wiescher, M., et al. 2017, RvMP, 89, 035007
Di Carlo, U. N., Giacobbo, N., Mapelli, M., et al. 2019, MNRAS, 487, 2947
Di Carlo, U. N., Mapelli, M., Bouffanais, Y., et al. 2020a, MNRAS, 497, 1043
Di Carlo, U. N., Mapelli, M., Giacobbo, N., et al. 2020b, MNRAS, 498, 495
Dominik, M., Belczynski, K., Fryer, C., et al. 2012, ApJ, 759, 52
Evans, M., Hastings, N., & Peacock, B. 2000, Statistical Distributions (3rd ed.; Hoboken, NJ: Wiley)
Farmer, R. 2018, rjfarmer/mesaplot, v1.0.8, Zenodo, doi:10.5281/zenodo.1441329
Farmer, R., & Bauer, E. B. 2018, rjfarmer/pyMesa: Add support for 10398, v1.0.3, Zenodo, doi:10.5281/zenodo.1205271
Farmer, R., Fields, C. E., Petermann, I., et al. 2016, ApJS, 227, 22
Farmer, R., Fields, C. E., & Timmes, F. X. 2015, ApJ, 807, 184
Farmer, R., Renzo, M., de Mink, S. E., Marchant, P., & Justham, S. 2019, ApJ, 887, 53
Farr, W. M., Fishbach, M., Ye, J., & Holz, D. E. 2019, ApJL, 883, L42
Ferguson, J. W., Alexander, D. R., Allard, F., et al. 2005, ApJ, 623, 585

Fernández, R., Quataert, E., Kashiyama, K., & Coughlin, E. R. 2018, MNRAS, 476, 2366
Fields, C. E., Farmer, R., Petermann, I., Iliadis, C., & Timmes, F. X. 2016, ApJ, 823, 46
Fields, C. E., Timmes, F. X., Farmer, R., et al. 2018, ApJS, 234, 19
Fishbach, M., Farr, W. M., & Holz, D. E. 2020, ApJL, 891, L31
Fishbach, M., & Holz, D. E. 2017, ApJL, 851, L25
Fishbach, M., Holz, D. E., & Farr, B. 2017, ApJL, 840, L24
Fowler, W. A., & Hoyle, F. 1964, ApJS, 9, 201
Fragione, G., & Kocsis, B. 2018, PhRvL, 121, 161103
Fraley, G. S. 1968, Ap&SS, 2, 96
Friščić, I., Donnelly, T. W., & Milner, R. G. 2019, PhRvC, 100, 025804
Fruet, G., Courtin, S., Heine, M., et al. 2020, PhRvL, 124, 192701
Fryer, C. L. 1999, ApJ, 522, 413
Fryer, C. L., Belczynski, K., Wiktorowicz, G., et al. 2012, ApJ, 749, 91
Fryer, C. L., & Warren, M. S. 2004, ApJ, 601, 391
Fryer, C. L., Woosley, S. E., & Heger, A. 2001, ApJ, 550, 372
Fuller, G. M., Fowler, W. A., & Newman, M. J. 1985, ApJ, 293, 1
Gerosa, D., & Berti, E. 2017, PhRvD, 95, 124046
Gerosa, D., & Berti, E. 2019, PhRvD, 100, 041301
Gilkis, A., Soker, N., & Papish, O. 2016, ApJ, 826, 178
Gomez, S., Berger, E., Nicholl, M., et al. 2019, ApJ, 881, 87
Graham, M. J., Ford, K. E. S., McKernan, B., et al. 2020, PhRvL, 124, 251102
Hamann, W. R., & Koesterke, L. 1998, A&A, 335, 1003
Hamann, W.-R., Koesterke, L., & Wessolowski, U. 1995, A&A, 299, 151
Hamann, W.-R., Schoenberner, D., & Heber, U. 1982, A&A, 116, 273
Hammache, F., Oulebsir, N., Roussel, P., et al. 2016, JPhCS, 665, 012007
Hammer, J. W., Fey, M., Kunz, R., et al. 2005, NuPhA, 752, 514
Heger, A., Fryer, C. L., Woosley, S. E., Langer, N., & Hartmann, D. H. 2003, ApJ, 591, 288
Heger, A., & Woosley, S. E. 2002, ApJ, 567, 532
Heger, A., Woosley, S. E., Rauscher, T., Hoffman, R. D., & Boyes, M. M. 2002, NewAR, 46, 463
Heger, A., Woosley, S. E., & Spruit, H. C. 2005, ApJ, 626, 350
Hoffman, R. D., Woosley, S. E., Weaver, T. A., Rauscher, T., & Thielemann, F. K. 1999, ApJ, 521, 735
Holt, R. J., Filippone, B. W., & Pieper, S. C. 2018, arXiv:1809.10176
Holt, R. J., Filippone, B. W., & Pieper, S. C. 2019, PhRvC, 99, 055802
Holz, D. E., & Hughes, S. A. 2005, ApJ, 629, 15
Hummel, J. A., Pawlik, A. H., Milosavljević, M., & Bromm, V. 2012, ApJ, 755, 72
Hunter, J. D. 2007, CSE, 9, 90
Iglesias, C. A., & Rogers, F. J. 1993, ApJ, 412, 752
Iglesias, C. A., & Rogers, F. J. 1996, ApJ, 464, 943
Iliadis, C., Champagne, A., José, J., Starrfield, S., & Tupper, P. 2002, ApJS, 142, 105
Iliadis, C., Longland, R., Champagne, A. E., & Coc, A. 2010a, NuPhA, 841, 251
Iliadis, C., Longland, R., Champagne, A. E., Coc, A., & Fitzgerald, R. 2010b, NuPhA, 841, 31
Itoh, N., Hayashi, H., Nishikawa, A., & Kohyama, Y. 1996, ApJS, 102, 411
Kimball, C., Talbot, C., Berry, C. P. L., et al. 2020, ApJ, 900, 177
Kluyver, T., Ragan-Kelley, B., Pérez, F., et al. 2016, in Positioning and Power in Academic Publishing: Players, Agents and Agendas: Proc. 20th Int. Conf. on Electronic Publishing, ed. F. Loizides & B. Schmidt (Amsterdam: IOS Press), 87
Kulkarni, S. R., Hut, P., & McMillan, S. 1993, Natur, 364, 421
Kunz, R., Fey, M., Jaeger, M., et al. 2002, ApJ, 567, 643
Langanke, K., & Martínez-Pinedo, G. 2000, NuPhA, 673, 481
Leung, S.-C., Nomoto, K., & Blinnikov, S. 2019, ApJ, 887, 72
LIGO Scientific Collaboration, Aasi, J., Abbott, B. P., et al. 2015, CQGra, 32, 074001
Lippuner, J., & Roberts, L. F. 2017, ApJS, 233, 18
Longland, R., Iliadis, C., Champagne, A. E., et al. 2010, NuPhA, 841, 1
Lovegrove, E., & Woosley, S. E. 2013, ApJ, 769, 109
Lunnan, R., Fransson, C., Vreeswijk, P. M., et al. 2018, NatAs, 2, 887
Mandel, I. 2010, PhRvD, 81, 084029
Mandel, I., & de Mink, S. E. 2016, MNRAS, 458, 2634
Mandel, I., Farr, W. M., & Gair, J. R. 2019, MNRAS, 486, 1086
Mangiagli, A., Bonetti, M., Sesana, A., & Colpi, M. 2019, ApJL, 883, L27
Marchant, P., Langer, N., Podsiadlowski, P., Tauris, T. M., & Moriya, T. J. 2016, A&A, 588, A50
Marchant, P., Renzo, M., Farmer, R., et al. 2019, ApJ, 882, 36
McKernan, B., Ford, K. E. S., Bellovary, J., et al. 2018, ApJ, 866, 66
Metcalfe, T. S. 2003, ApJL, 587, L43
Metcalfe, T. S., Salaris, M., & Winget, D. E. 2002, ApJ, 573, 803
Metcalfe, T. S., Winget, D. E., & Charbonneau, P. 2001, ApJ, 557, 1021
Nadezhin, D. K. 1980, Ap&SS, 69, 115
Nicholl, M., Blanchard, P. K., Berger, E., et al. 2020, NatAs, 4, 893
Nitz, A. H., Dent, T., Davies, G. S., et al. 2020, ApJ, 891, 123
Oda, T., Hino, M., Muto, K., Takahara, M., & Sato, K. 1994, ADNDT, 56, 231
Pastorello, A., Smartt, S. J., Mattila, S., et al. 2007, Natur, 447, 829
Paxton, B., Bildsten, L., Dotter, A., et al. 2011, ApJS, 192, 3
Paxton, B., Cantiello, M., Arras, P., et al. 2013, ApJS, 208, 4
Paxton, B., Marchant, P., Schwab, J., et al. 2015, ApJS, 220, 15
Paxton, B., Schwab, J., Bauer, E. B., et al. 2018, ApJS, 234, 34
Paxton, B., Smolec, R., Schwab, J., et al. 2019, ApJS, 243, 10
Pérez, F., & Granger, B. E. 2007, CSE, 9, 21
Pols, O. R., Tout, C. A., Eggleton, P. P., & Han, Z. 1995, MNRAS, 274, 964
Portegies Zwart, S. F., & McMillan, S. L. W. 2000, ApJ, 528, L17
Potekhin, A. Y., & Chabrier, G. 2010, CoPP, 50, 82
Quataert, E., Lecoanet, D., & Coughlin, E. R. 2019, MNRAS, 485, L83
Rakavy, G., & Shaviv, G. 1967, ApJ, 148, 803
Rauscher, T., Nishimura, N., Hirschi, R., et al. 2016, MNRAS, 463, 4153
Rauscher, T., & Thielemann, F.-K. 2000, ADNDT, 75, 1
Regős, E., Vinkó, J., & Ziegler, B. L. 2020, ApJ, 894, 94
Renzo, M., Farmer, R., Justham, S., et al. 2020a, A&A, 640, A56
Renzo, M., Farmer, R. J., Justham, S., et al. 2020b, MNRAS, 493, 4333
Rockefeller, G., Fryer, C. L., & Li, H. 2006, arXiv:astro-ph/0608028
Rodriguez, C. L., Amaro-Seoane, P., Chatterjee, S., et al. 2018, PhRvD, 98, 123005
Rodriguez, C. L., Chatterjee, S., & Rasio, F. A. 2016, PhRvD, 93, 084029
Rodriguez, C. L., Zevin, M., Amaro-Seoane, P., et al. 2019, PhRvD, 100, 043027
Rogers, F. J., & Nayfonov, A. 2002, ApJ, 576, 1064
Roupas, Z., & Kazanas, D. 2019, A&A, 632, L8
Salaris, M., Domínguez, I., García-Berro, E., et al. 1997, ApJ, 486, 413
Sallaska, A. L., Iliadis, C., Champange, A. E., et al. 2013, ApJS, 207, 18
Salvatier, J., Wieckiâ, T. V., & Fonnesbeck, C. 2016, PyMC3: Python Probabilistic Programming Framework, v3.7, Astrophysics Source Code Library, ascl:1610.016
Saumon, D., Chabrier, G., & van Horn, H. M. 1995, ApJS, 99, 713
Schutz, B. F. 1986, Natur, 323, 310
Shen, Y. P., Guo, B., deBoer, R. J., et al. 2020, PhRvL, 124, 162701
Spera, M., Mapelli, M., Giacobbo, N., et al. 2019, MNRAS, 485, 889
Stone, N. C., Metzger, B. D., & Haiman, Z. 2017, MNRAS, 464, 946
Stothers, R. B. 1999, MNRAS, 305, 365
Straniero, O., Domínguez, I., Imbriani, G., & Piersanti, L. 2003, ApJ, 583, 878
Sukhbold, T., & Adams, S. 2020, MNRAS, 492, 2578
Takahashi, K. 2018, ApJ, 863, 153
Tan, W. P., Boeltzig, A., Dulal, C., et al. 2020, PhRvL, 124, 192702
Thielemann, F.-K., Nomoto, K., & Hashimoto, M.-A. 1996, ApJ, 460, 408
Timmes, F. X., & Swesty, F. D. 2000, ApJS, 126, 501
Toro, E. F., Spruce, M., & Speares, W. 1994, ShWav, 4, 25
Townsend, R. 2019, MESA SDK for Linux: 20180822, Zenodo, doi:10.5281/zenodo.2603170
Tumino, A., Spitaleri, C., La Cognata, M., et al. 2018, Natur, 557, 687
Tur, C., Heger, A., & Austin, S. M. 2007, ApJ, 671, 821
Tutukov, A. V., & Yungelson, L. R. 1993, MNRAS, 260, 675
Udall, R., Jani, K., Lange, J., et al. 2020, ApJ, 900, 80
van der Walt, S., Colbert, S. C., & Varoquaux, G. 2011, CSE, 13, 22
van Son, L. A. C., De Mink, S. E., Broekgaarden, F. S., et al. 2020, ApJ, 897, 100
Vigna-Gómez, A., Justham, S., Mandel, I., de Mink, S. E., & Podsiadlowski, P. 2019, ApJL, 876, L29
Villar, V. A., Nicholl, M., & Berger, E. 2018, ApJ, 869, 166
Vitale, S., Lynch, R., Raymond, V., et al. 2017, PhRvD, 95, 064053
Weaver, T. A., & Woosley, S. E. 1993, PhR, 227, 65
West, C., Heger, A., & Austin, S. M. 2013, ApJ, 769, 2
Whalen, D. J., Even, W., Frey, L. H., et al. 2013b, ApJ, 777, 110
Whalen, D. J., Fryer, C. L., Holz, D. E., et al. 2013a, ApJL, 762, L6
Woosley, S. E. 2017, ApJ, 836, 244
Woosley, S. E. 2018, ApJ, 863, 105
Woosley, S. E. 2019, ApJ, 878, 49
Woosley, S. E., Blinnikov, S., & Heger, A. 2007, Natur, 450, 390
Woosley, S. E., & Heger, A. 2007, PhR, 442, 269
Woosley, S. E., Heger, A., & Weaver, T. A. 2002, RvMP, 74, 1015
Woosley, S. E., Timmes, F. X., & Weaver, T. A. 1993, JPhG, 19, S183
Yang, Y., Bartos, I., Gayathri, V., et al. 2019, PhRvL, 123, 181101
Yoshida, T., Umeda, H., Maeda, K., & Ishii, T. 2016, MNRAS, 457, 351
Young, D. R., Smartt, S. J., Mattila, S., et al. 2008, A&A, 489, 359